Geophysical Journal International

Geophys. J. Int. (2025) **244,** 1–18
Advance Access publication 2025 November 19
Research Paper

https://doi.org/10.1093/gji/ggaf448

Dependence of Archie's saturation exponent on hydrate saturation and hydrate morphology: a study from fluid-displacing and fracture-filling hydrate reservoirs

Xiangyu Zhu,[1,2] Sourav K. Sahoo∗,[3] Zhenyu Zhu,[1] Weixin Pang,[1,2] Lixia Li,[1,2]
Erik Spangenberg,[4] Klaus Bauer[4] and Angus I. Best[3]

[1] *CNOOC Research Institute Co., Ltd, Beijing 100028, China*
[2] *State Key Laboratory of Offshore Natural Gas Hydrates, Beijing 102209, China*
[3] *National Oceanography Centre, Southampton SO143ZH, UK. E-mail:* s.sahoo@noc.ac.uk
[4] *GFZ Helmholtz Centre for Geosciences,* Potsdam 14473, *Germany*

Accepted 2025 November 5. Received 2025 November 5; in original form 2025 May 27

SUMMARY

Accurate quantification of natural gas hydrate is essential for resource potential and climate impact assessment. Archie's empirical equations are commonly used to quantify hydrates from electrical resistivity measurements. One dominant Archie equation parameters, that is, saturation parameter (n), is generally assumed to be constant for different hydrate saturation range for a given reservoir. However, n actually varies with hydrate saturation and morphology, and the exact relationship between n and hydrate saturation or morphology still remains poorly understood, leading to great uncertainties in resistivity-derived saturations. Here we investigate the effect of hydrate saturation and dominant hydrate morphologies on n using well logs from four sites in both fine and coarse-grained sediments: two sites with fluid-displacing hydrate (site W11 from the third Guangzhou Marine Geologic Survey; and Mallik 5L-38 well in the Mackenzie Delta) and two sites with fracture-filling hydrate (site 10 from Indian National Gas Hydrate Program Expedition 01; and site W08 from the second Guangzhou Marine Geologic Survey). We calculated n value using Archie's law with hydrate saturation determined from velocity. Our results demonstrate a clear negative relationship between hydrate content and n value. Moreover, n estimates from two fracture-filling sites show greater variability compared to fluid-displacing sites. At a fracture-filling hydrate site, site 10, various trends between n and hydrate saturation are possibly caused by the distinct gas compositions of hydrate. Our results demonstrate that significant effects of hydrate morphology and saturation on n that are site specific, and can be used to enhance the accuracy of gas hydrate quantification.

Key words: Numerical modelling; Downhole methods; Gas and hydrate systems.

1 INTRODUCTION

Natural gas hydrates exist as ice-like solid compounds formed under suitable high-pressure and low-temperature conditions if sufficient gas (mostly Methane) and water is available, and are found globally in terrestrial permafrost and offshore sediment (Kvenvolden 1993). Gas hydrate has been of interest as a clean energy resource for decades but significant challenges still remain for commercial production (Milkov *et al.* 2003; Collett *et al.* 2009). On the other hand, hydrate dissociation is usually evaluated as a potential cause for geohazards such as landslides. Gas products of the dissociation can contribute to global warming and impose challenges to the environment if it releases into the atmosphere (e.g. Kvenvolden & Lorenson 2001; Paull *et al.* 2008). Recently, artificial gas hydrate has been assessed as a possible solution for carbon dioxide sequestration (e.g. Sahoo & Best 2021; Yu *et al.* 2021).

Hydrate grains can distribute in distinct modes (i.e. morphologies) within a rock or sediment composed of mineral grains and pore fluid. Holland *et al.* (2008) studied the morphology of natural gas hydrate from core samples, categorizing it into two types: (i) fluid-displacing (i.e. pore-filling, hydrate grains replace the pore fluid) and (ii) grain-displacing (hydrate grains replace solid mineral grains). Experiments on synthetic hydrate and petrophysical inversion from field measurements further indicate or imply a number of subtypes of hydrate microstructure. For example, fluid-displacing hydrate can (i) fill in the pore, (ii) bond the mineral grains (i.e. cementing morphology), (iii) float within pore space without contact with sediment grains (i.e. pore-floating) or (iv) be part of the solid matrix (i.e. pore-bridging, load-bearing), while grain-displacing hydrate in fracture-dominated reservoirs may accumulate in the shape of (i) nodules or (ii) veins normally aligned to minimum principal stress (Dai *et al.* 2012; Sahoo *et al.* 2018a) and are commonly associated with fine grained sediments (Booth *et al.* 1998). In natural systems, so far, the load-bearing and vein-like (i.e. fracture-filling) morphologies are the most common fluid-displacing and grain-displacing forms of hydrate, respectively (e.g. Helgerud *et al.* 1999; Dai *et al.* 2008; Kim *et al.* 2013; Collett *et al.* 2015; Sha *et al.* 2015).

The amount of natural gas hydrate is usually estimated from hydrocarbon-sensitive geophysical properties, for example, electrical resistivity and/or elastic wave velocity (Li & Liu 2016, 2020). The nonlinear relationship between hydrate content and electrical resistivity, as described by the relations of Archie (1942), largely relies on an empirical saturation parameter n. For gas hydrates, both laboratory measurements and field studies show that n usually varies from reservoir to reservoir. For example, a saturation exponent $n = 1.9386$, determined from an analogue experiment on ice-bearing sediment (Pearson *et al.* 1983), was commonly used to quantify the hydrate at several marine and permafrost sites (e.g. Paull *et al.* 1996). Santamarina & Ruppel (2008) and Dallimore *et al.* (1999) estimated $n = 1.6$ was the best fit for electrical conductivity of tetrahydrofuran hydrate formed in sand, silts and clay samples. Cook & Waite (2018) employed calibrated n values ranging from 1.5 to 2.5 to interpret the resistivity anomalies induced by fluid-displacing hydrate within two isotropic coarse-grained reservoirs. Theoretical modelling for vein-like hydrates deposited in fracture-dominated reservoirs (e.g. Kennedy & Herrick 2004), where the resistivity is sensitive to the direction of measurement, indicated a wider range of n between 1.25 and 7. Various factors can account for the site-specific saturation exponent within hydrate-bearing sediment. Experimental and theoretical investigations have shown that non-hydrocarbon factors such as host sediment properties (pore shape, pore connectivity, clay content) and fluid distribution mode can significantly affect the saturation exponent (e.g. Worthington & Pallatt 1992; Schön 1996; Sen 1997; Wildenschild *et al.* 2000).

Additionally, for a given site, the Archie parameters vary with hydrate saturation and morphology. Modelling of Spangenberg (2001) indicated the factors determining the saturation exponent n may vary between distinct hydrate morphologies: (i) n for disseminated fluid-displacing hydrate-bearing sediment can largely depend on grain size and grain size sorting as a result of capillary effects (Clennell *et al.* 1999), and (ii) the value of n for nodular or horizontally layered grain-displacing hydrate-bearing sediment relies on the relationship between porosity and formation resistivity factor (i.e. Archie's cementation exponent m). However, many of the field studies use a single value of n for the whole hydrate saturation range at a given site (e.g. Collett *et al.* 2003; Collett & Lee 2005; Riedel *et al.* 2006; Wang *et al.* 2011), which is not always correct. Moreover, only a handful studies have accounted for the changes of n with hydrate saturation. For example, recent work by Cook & Waite (2018) using field data from Mallik 5L-38 and Gulf of Mexico showed n varies with S_h giving $n = 2.5 \pm 0.5$ for coarse-grained sediments with hydrate saturation above 40 per cent. They also point out that 'if possible, n should be calibrated using reservoir-specific data'. Overall, the mechanisms that control how hydrate-related factors (e.g. hydrate content and morphology) impact the saturation exponent have not been fully understood from either field or laboratory measurements.

In this work we aim to investigate the effect of the two most dominant hydrate-related factors affecting the saturation exponent, namely hydrate saturation and hydrate morphology. We look at both coarse-grained and fine-grained sediments and aim to provide a mathematical relationship between n and S_h. We use downhole logs collected from four reservoirs where either fluid-displacing or fracture-filling hydrate were observed. Site 10 from the Indian National Gas Hydrate Program Expedition 01 (NGHP01) in the Bay of Bengal, and well W08 in the South China Sea from the second Guangzhou Marine Geologic Survey (GMGS2) were selected as examples of fracture-filling reservoirs, while the Mallik Gas Hydrate Production Research Well, Mallik 5L-38, in Canada, and well W11 in the South China Sea from the third Guangzhou Marine Geologic Survey (GMGS3) are used as examples of fluid-displacing reservoirs. First, we use the velocity logs from those depth intervals where hydrates were present to calculate the hydrate saturation using well-established rock physics models. These elastic wave velocity-derived hydrate contents are then used as input to calculate the saturation exponents from electrical resistivity measurements using Archie's equation. Finally, cross-plots of saturation exponent and hydrate saturation are employed to illustrate the dependence of saturation exponent on morphologies and hydrate content. We also investigated the influences of conductive clay particles and uncertainties in calculations on n values.

2 HYDRATE SATURATION ESTIMATION

Besides the electrical resistivity, other geophysical measurements such as elastic wave velocity and nuclear magnetic resonance (NMR), as well as geochemical measurements of chloride concentration, can provide independent estimates of gas hydrate saturation. Estimation based on velocity data largely depends on the conceptual model (i.e. rock physics model) that links the petrophysical properties, here the composition of the pore content, to the rock elastic properties. When utilizing rock physic models for hydrate quantification, parameters and petrophysical properties involved in modelling should be carefully selected as they can also significantly affect the predicted velocity. In contrast, for NMR tools, pressure core and chloride concentration the measurements mainly relate to the hydrate content, independent of the pore-scale interactions between gas hydrate and the host sediments; therefore, they are assumed to be able to provide more accurate concentrations of *in situ* gas hydrate than information derived from seismic or sonic velocities (e.g. Lee 2007). However, during downhole surveys, NMR logging, pressure core and chloride measurement are not usually deployed due to the high operational and time costs and failure risk (Coates *et al.* 1999). Moreover, chloride concentrations from core samples tend to be quite dispersed in-depth. Inspired by the method of Cook & Waite (2018), here we propose to calculate the hydrate saturation from sufficient velocity measurements, and then employ them for further n calculation only if these saturation estimates match the predictions from available NMR or salinity data.

2.1 Saturation from velocity

Rock physics models specify the relationships between rock petrophysical and elastic properties, and are commonly used to obtain hydrate saturation from velocity measurements. In hydrate-bearing sediment, the geometry of hydrate grains (i.e. morphology) is an

Table 1. Constants involved in velocity modelling.

Constituent	K (GPa)	G (GPa)	ρ(g cm^{-3})	Source
Quartz	38.4	44.1	2.66	Pabst & Gregorová (2013)
Clay	20.9	6.85	2.58	Helgerud *et al.* (1999)
Gas hydrate	8.3	3.54	0.924	Helgerud *et al.* (2009)
Sea water	2.3	0	1.02	Cook & Waite (2018)

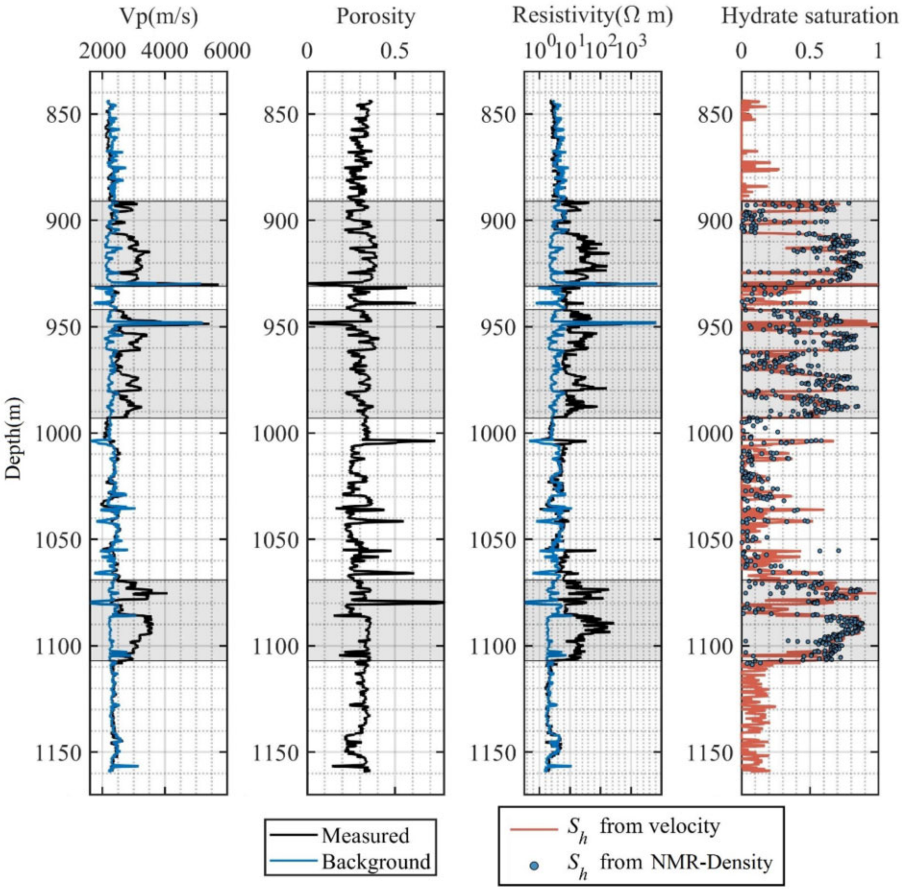

Figure 1. Compressional wave velocity (V_P), porosity, resistivity and hydrate saturation at site Mallik 5L-38. Measured V_P and resistivity are from original drilling report (Collett, Lewis, Dallimore 2005). We calculated porosities from the LWD density log. The hydrate saturations estimated from NMR-density porosity are from Kleinberg *et al.* (2005) and shown as blue dots. We calculated the background V_P and resistivity (V_P and resistivity of the sediments after replacing hydrates with brine) and showed them in blue curves. We estimated the hydrate saturations from velocity and shown them in the red curve. Three noteworthy gas hydrate-bearing intervals, as highlighted in grey, are 891–931, 942–993 and 1069–1107 m. The mean of absolute difference between velocity-derived S_h and NMR-density-derived S_h is 8 per cent. Tortuosity coefficient a and cementation exponent m for Archie's law are 0.65 and 2.23, respectively.

essential element when designing a rock physics model (e.g. Helgerud *et al.* 1999); an inappropriate conceptual model could result in a large deviation between velocity-derived and *in situ* hydrate saturations (e.g. Lee & Collett 2009). Here, we use two morphology-related rock physics models to quantify the hydrate in four reservoirs where each accumulates either fluid-displacing or fracture-filling hydrate.

2.1.1 *Fluid-displacing sites*

Dvorkin *et al.* (2000) investigated the elastic properties of sediments hosting fluid-displacing hydrate by proposing four effective medium models, which assume the hydrate (i) floats within the pore fluid (pore-floating), (ii) constitutes part of the solid matrix with mineral grains (load-bearing), (iii) coats the mineral grains (grain-coating) or (iv) cements the mineral grains at grain contacts (contact-cementing). Different from the empirical time-average-relation by Wyllie *et al.* (1956) or its adjustment to hydrate-bearing soft sediment (weighted time-average-relation) by Lee *et al.* (1996), these morphology-related models are based on first principal physics (Dvorkin & Nut 1998) and require limited parameters to recalibrate when applied in a new reservoir. Of these models, the load-bearing type has been widely validated by both laboratory and field measurements from marine and permafrost environments (e.g. Kleinberg *et al.* 2005; Santamarina *et al.* 2015). Here we employ this model to quantify the fluid-displacing hydrate at sites Mallik 5L-38 and W11, GMGS3.

Using the porosity log and constant parameters listed in Table 1, we calculate the background (hydrate-free) V_P at both sites (see blue curves in the first logs of Figs 1 to 3). The procedure has been

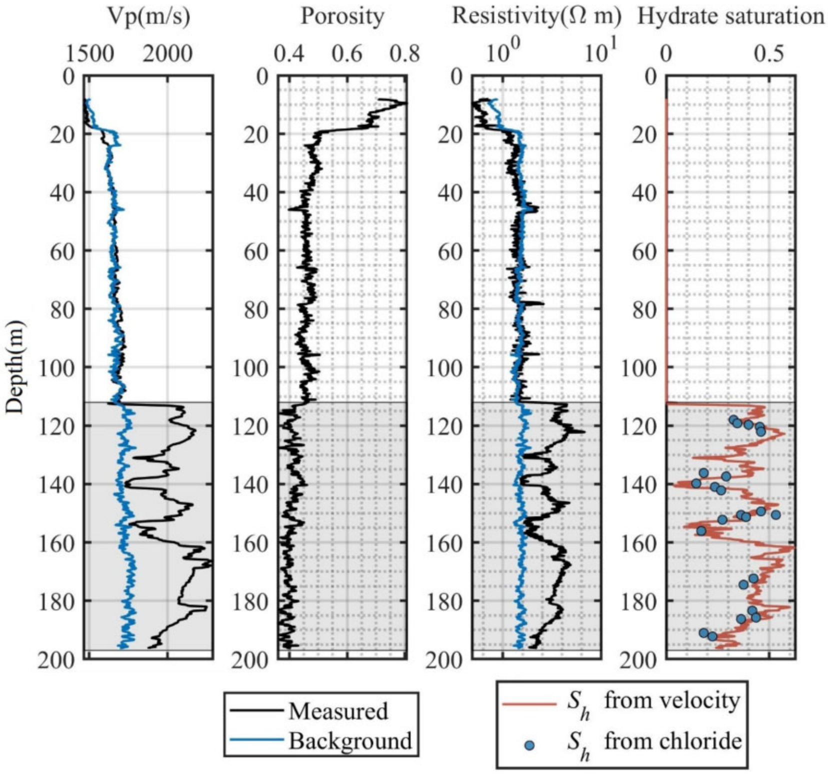

Figure 2. Compressional wave velocity (V_P), porosity, resistivity and hydrate saturation at site W11, GMGS3. LWD V_P and resistivity data are from Qian *et al.* (2018). We calculated the background V_P and resistivity (V_P and resistivity of the sediments after replacing hydrates with brine) and showed them in blue curves. We calculated porosities from the LWD density log. Hydrate saturations calculated from chloride concentration are from Qian *et al.* (2018) and shown as blue dots. We estimated the hydrate saturations from velocity and shown them in the red curve. The hydrate-bearing interval used in this study, as indicated by the grey zone, is from 116 to 201 mbsf. The mean of absolute difference between velocity-derived S_h and NMR-density-derived S_h is 6 per cent. Tortuosity coefficient a and cementation exponent m for Archie's law are 1.78 and 1.57, respectively.

illustrated by Tian & Liu (2021). At Mallik 5L-38, three typical gas hydrate-bearing intervals (shown as grey zones in Fig. 1) are indicated by the obvious deviation between the background and measured V_P (Collett & Lee 2005). Massive gas hydrate (a maximum saturation of ∼90 per cent) is predicted from velocity measurements in all three intervals. At the other fluid-displacing hydrate site, W11 from GMGS3, the predicted background V_P in Fig. 2 conforms well to the measured V_P, except within the interval from 116 to 201 m below seafloor (mbsf), where a significant velocity increase is attributed to gas hydrate occurrence. The good agreement of the measured and calculated velocities in the hydrate-free zones confirms that the formation is well described by the chosen parameters. A large amount of hydrate, with saturation up to 60 per cent, is estimated from the velocity within the hydrate-bearing interval.

2.1.2 Fracture-filling sites

Fracture-filling hydrates at sites GMGS2-W08 and NGHP01-10 mainly appear in the shape of veins or tubes but form under different mechanisms (Cook *et al.* 2010; Luo & Cao 2023). For site NGHP01-10 fracture-filling hydrates are present almost exclusively in one depth interval, slightly above and unconnected to the base of the gas hydrate stability zone (GHSZ). This suggests that, *in situ* microbial gas is inferred gas source for such vein-like hydrates (Cook & Goldberg 2008). In contrast, at site GMGS2-W08 fractures provide the path for gassy fluid migration; free gas from deeper locations possibly supplies the gas for hydrate accumulation (Sha *et al.* 2015).

Vein-like hydrates in reservoirs usually result in the anisotropy of rock elastic and electrical properties. Lee & Collett (2009) characterize the hydrate-induced elastic anisotropy using a two-layer-laminated, transversely isotropic model, in which the hydrate and background sediment constitute two individual layers. In that model the anisotropic elastic wave velocities are computed using a specific average form of pure hydrate moduli and background sediment moduli (i.e. White 1965). Generally pure hydrate elastic moduli are calibrated by laboratory measurements (e.g. constants shown in Table 1). In the case of the brine-saturated part, we compute its moduli using the scheme from Dvorkin *et al.* (2000), which we used for fluid-displacing hydrate at Mallik 5L-38 and W11-GMGS3 as well. We chose not to model the properties of the brine-saturated part with another commonly used scheme, a modified Biot model by Lee (2008), because increasing differences between rock physics models for fracture-filling and fluid-displacing hydrates would contribute to more uncertainties in the derived saturations.

In addition to the porosity and mineral properties (listed in Table 1), fracture dip is required in the elastic modelling of fracture-filling-hydrate in sediment. Core samples observations and resistivity-at-the-bit images at site NGHP01-10 indicated that fractures filled with hydrate are usually sub-vertical, with high-angle dip (e.g. Lee & Collett 2009; Cook *et al.* 2010). At site GMGS2-W08, near-vertical fractures are inferred to be part of a venting system, and free gas below the gas hydrate stability zone moves upwards through these pathways. During the migration process, a proportion

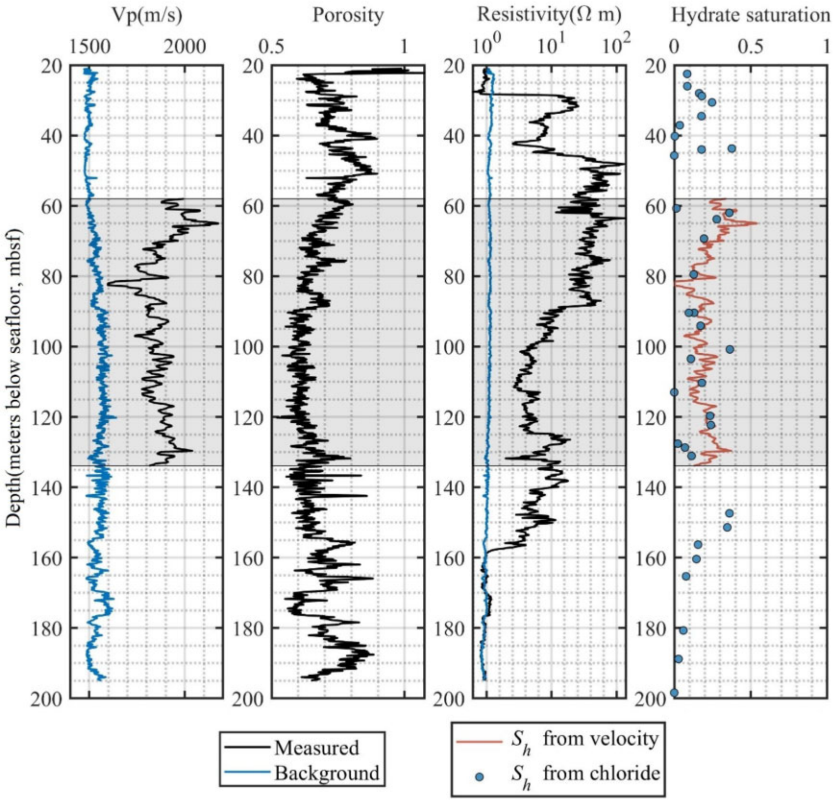

Figure 3. Compressional wave velocity (V_P), porosity, resistivity and hydrate saturation at site 10, NGHP01. Wireline V_P log was collected at Hole 10D while LWD resistivity was measured at Hole 10A (Lee & Collett 2009). We calculated background V_P and resistivity (V_P and resistivity of the sediments after replacing hydrates with brine) and showed them in blue curves. We estimated porosities using the wireline density log at Hole 10A. We calculated hydrate saturations from chloride concentration are shown as blue dots. We also calculated the hydrate saturations from velocity and shown them in the red curve. The hydrate-bearing interval used in this study, as indicated by grey zone, is from 58 to 134 mbsf. The mean of absolute difference between velocity-derived S_h and NMR-density-derived S_h is 10 per cent. Tortuosity coefficient *a* and cementation exponent *m* for Archie's law are 4.19 and 0.46, respectively.

of the free gas can form the sub-vertical hydrate veins and thick hydrate layers (Sha *et al.* 2015). Given these demonstrations, in this work we assume hydrate veins and layers are vertical to fracture normal when estimating hydrate saturation from velocities at both sites.

For site NGHP01-10, one logging while drilling (LWD) hole, Hole 10A, and one wireline logging hole, Hole 10D were drilled with closely spaced. Given a much shorter time lapse between drilling and data collecting for LWD measurements, we choose LWD rather than wireline logs for hydrate saturation estimation. However, a comparison between measurements from Hole 10A and 10D have shown that LWD velocities are much lower than wireline velocities at hydrate intervals but approach wireline velocities within hydrate-free intervals. The possible reason could be the hydrate dissociation caused by drilling disturbance (Lee & Collett 2009): drilling process can possibly cause the hydrate dissociation, and the released free gas can significantly lower the LWD *P*-wave velocity measurements. Regarding the biased LWD velocity, we employ the wireline velocity from Hole 10D to estimate hydrate saturation. However, velocity at Hole 10D cannot be used to calibrate the parameters of rock physics model (e.g. coordination number) as it was only collected at hydrate intervals. In contrast, LWD velocity measurements at Hole 10A covered both hydrate-free and hydrate-bearing intervals; therefore, we use *P*-wave velocity within hydrate-free intervals at Hole 10A to calibrate model parameters before hydrate saturation calculation.

In Fig. 3, the velocity log at site NGHP01-10 is only available from 58 to 134 mbsf, a narrower interval than that of other downhole measurements such as resistivity and porosity. In this velocity-available interval the estimated background V_P is much lower than measured V_P, indicating possible hydrate presence in this depth range. Results from downhole resistivity measurement further confirm it: high gas hydrate accumulation, indicated by significant resistivity increase, can be inferred between 30 and 360 mbsf. Using the velocity measurements from 58 to 134 mbsf, site NGHP01-10, we estimate the *in situ* hydrate concentration which ranges from 10 per cent to 55 per cent.

At the other fracture-filling hydrate site, GMGS2-W08, the predicted hydrate-free V_P and measured V_P coincide very well at shallow and deep depths, but diverge within the middle interval, from 65 to 98 mbsf. Hydrate presence accounts for the divergence between the measured and calculated logs. From velocity difference we estimated the hydrate content for this interval, which varies from 0 per cent to 51 per cent.

2.2 Saturation from nuclear magnetic resonance, pressure core and geochemistry measurements

The difference between density-derived and NMR-derived porosities can reflect the hydrate content (e.g. Kleinberg *et al.* 2005) as

(i) porosity measured by the NMR tool is highly related to the water porosity (the ratio of the volume of water to the volume of whole rock) and (ii) porosity derived from density measurements is the sum of water porosity and gas hydrate porosity (the ratio of the volume of gas hydrate to the volume of whole rock). Besides, a geochemical analysis, the measurement of pore fluid chloride concentration, is widely employed to provide accurate hydrate saturation estimates (e.g. Froelich *et al.* 1995; Hesse 2003). Gas hydrate saturations can also be estimated from the pressure core using the total amount of gas released during the depressurization experiment and the dissolved methane gas in the pore water under the assumption of a thermodynamic equilibrium (Lee & Collett 2009). On chloride concentration profile collected from recovered samples, hydrate is usually indicated by abnormally low chlorinity since hydrate dissociation freshens the pore fluids during core recovery.

Only the NMR log was collected at site Mallik 5L-38, while the chloride concentration was measured from the core samples at sites GMGS3-W11 and NGHP01-10. Both the pressure core and geochemistry measurement on core is available at site W08 during GMGS2. Hydrate contents estimated from available NMR, pressure core test and geochemistry measurements, as plotted by blue dots in Figs 1 to 3, are generally consistent with the velocity-derived hydrate concentrations. Given that, we consider these velocity-derived hydrate contents are reliable and hence can be used at all sites for further saturation exponent calibration.

3 ESTIMATION OF BACKGROUND RESISTIVITY R_0

The background geological formation's resistivity, denoted R_0, in hydrate-bearing intervals is usually derived using Archie's law and the resistivity collected in hydrate-free intervals, assuming that the pore water is the only conducting phase. According to Archie's equation shown below (Archie 1942), R_0 largely depends on the host sediment properties such as sediment porosity and brine conductivity:

$$R_0 = \frac{a R_w}{\phi^m}, \tag{1}$$

where a is the Archie tortuosity coefficient, R_w is the formation water resistivity at reservoir temperature and pressure, m is the Archie cementation exponent and ϕ is the sediment porosity calculated from density measurements.

Resistivity of *in situ* pore water R_w in eq. (1) is mainly a function of the temperature and dissolved salt content within the pore waters. In the case of seafloor sediment with known pore water temperature and salinity, R_w could be obtained by interpolating the measurement data provided by International Critical Tables of Numerical Data (1928). Then an empirical relationship is commonly employed to derive the R_w within subseafloor sediment at a certain depth (Arp 1953):

$$R_w^{\mathrm{subseafloor}} = R_w^{\mathrm{seafloor}} \frac{T_{\mathrm{seafloor}} + 7}{T_{\mathrm{subseafloor}} + 7}, \tag{2}$$

where T_{seafloor} and $T_{\mathrm{subseafloor}}$ are seafloor and subseafloor Fahrenheit temperatures, respectively. $T_{\mathrm{subseafloor}}$ could be calculated using available data for T_{seafloor} and the geothermal gradient. $R_w^{\mathrm{subseafloor}}$ and R_w^{seafloor} denote the pore water resistivities for seafloor and subseafloor sediments, respectively. These salinity and temperature parameters at all research wells except Mallik 5L-38 are given in Table 2. Mallik 5L-38 is an exception as the R_w there is more complex than other sites. Although previous studies of site Mallik 5L-38 (e.g. Collett & Dallimore 1998) have demonstrated sediments at depths from 200 to 2000 m have an average pore-water salinity about 10 parts per thousand (ppt), measurements from recovered cores show a highly variable pore-water salinity ranging from 1 ppt to up to 45 ppt (Matsumoto *et al.* 2005). In that case, a single salinity value would no longer be suitable to use. Here we employed the R_w provided by Collett & Lee (2005), who determined the baseline of R_w using a combination of downhole logs and pore-water salinity from core samples.

Using a and m determined from eq. (1) and R_w estimated from eq. (2), we calculate the background resistivity R_0 for all depth points. As shown in Figs 1 to 4, the hydrate-free intervals indicated by resistivity measurements and R_0 are consistent with those intervals predicted by velocity measurements and background velocities.

4 ESTIMATION OF SATURATION EXPONENT

Based on the calibrated R_0, we then obtain the saturation exponent according to the rearranged Archie second law:

$$n = \frac{-\log(I_R)}{\log(1 - S_h)} = \frac{\log(R_0/R_t)}{\log(1 - S_h)}, \tag{3}$$

where R_t represents the measured resistivity of the hydrate reservoir, S_h is the hydrate saturation estimated from velocities (see Section 2.1). I_R is the resistivity index, the ratio of the resistivity of the partial water-saturated rock (water saturation $S_w = 1 - S_h$) to the resistivity of fully electrolyte-saturated reservoir rock. Eq. (3) is generally useful for a given rock sample under the Archie experimental conditions, that is, fluid is required to be high-salinity (NaCl) brine with $S_w > 15$ per cent (Worthington & Pallatt 1992). In addition, low velocity-derived S_h (e.g. less than 10 per cent), mostly resulting from small gaps between estimated background V_P and measured V_P for brine-saturated sediments, can yield abnormally high n values according to eq. (3). Given these demonstrations, we only use the resistivity data with S_h ranging from 10 per cent to 85 per cent for further investigations.

5 DEPENDENCIES OF SATURATION EXPONENT

Fig. 5 depicts cross-plots of n and S_h for hydrate-bearing sediments at the four different sites. It can be seen that, for all sites, the increase of hydrate saturation generally results in decrease of the saturation exponent, especially for vertical-fractured sites NGHP01-10, and W08, GMGS2. In terms of the relationship between S_h and n, we tried three fitting strategies, linear, power function and exponential function regression for all four sites. R-squared values for n estimates are shown in Table 3. For sites Mallik 5L-38, W11, GMGS3 and W08-GMGS2, power function is the best fitting for the largest R-squared value. However, at site NGHP01-10, the trends between n and hydrate saturation within 58–95 mbsf (Interval I), 95–125 mbsf (Interval II) and 125–134 mbsf (Interval III) are quite distinct. We employ three fitting strategies for Intervals I–III independently, and find that the best fitting for Interval I is the power function but for Intervals II–III is the exponential function.

The n value estimates for fracture-filling sites are generally much higher and more scattered than those from fluid-displacing sites. For the two fluid-displacing hydrate sites, Mallik 5L-38 and W11-GMGS3, the estimated saturation exponents are generally under 10. Site Mallik 5L-38, with a wider range of hydrate saturation,

Table 2. Salinity and temperature parameters used for R_w estimation.

Sites	Seafloor temperature (°C)	Geothermal gradient (°C km^{-1})	Salinity (ppt)	Source
W11, GMGS3	4.82	54.9	32	Qian *et al.* (2018)
NGHP01-10	6.5	45	32.5	Lee & Collett (2009)
W08, GMGS2	4	45	35	Wang *et al.* (2016)

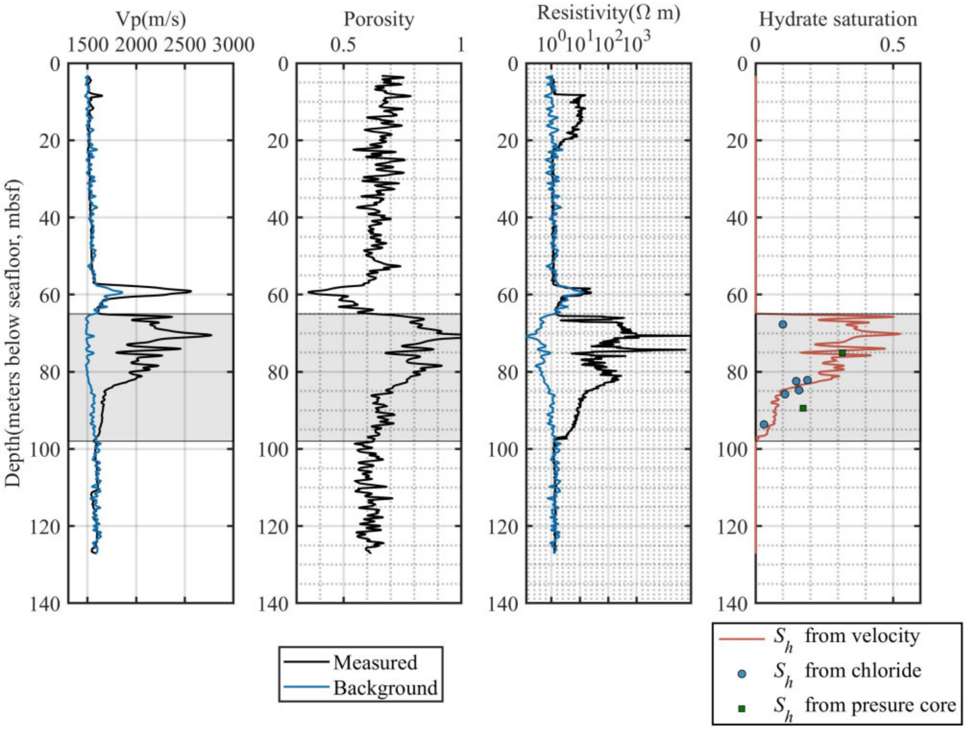

Figure 4. Compressional wave velocity (V_P), porosity, resistivity and hydrate saturation at site W08, GMGS2. LWD V_P and resistivity data were from Sha *et al.* (2015). We calculated background V_P and resistivity (V_P and resistivity of the sediments after replacing hydrates with brine) and showed them in blue curves. We calculated porosities from the LWD density log. We also calculated the hydrate saturations from velocity and showed them in the red curve. Hydrate saturations calculated from chloride and pressure core data are from Qian *et al.* (2017) and shown as blue and green markers, respectively. The hydrate-bearing interval used in this study, as indicated by grey zone, is from 65 to 98 mbsf. The mean of absolute difference between velocity-derived S_h and non-velocity-derived S_h (S_h from chloride and pressure core) is 11 per cent. Tortuosity coefficient *a* and cementation exponent *m* for Archie's law are 0.84 and 4, respectively.

is estimated to have more dispersed saturation exponents than site W11-GMGS3. As demonstrated in Fig. 6, 86.86 per cent of *n* estimates at site W11-GMGS3 are between 1 and 2, while the figure for site Mallik 5L-38 is merely 48.98 per cent. From the histograms in Fig. 6 we also observe that the *n* interval, from 1.5 to 2, is the range with the highest relative frequency for both sites, in accord with the *n* range suggested by Cook and Waite (2018). In the case of vertical-fracture-filling hydrate, *n* predictions from sites NGHP01-10 and GMGS2-W08 primarily vary from 3 to 30. Histograms in Fig. 6 indicate *n* at site NGHP01-10 is within much lower intervals compared to that at site GMGS2-W08. For example, at site NGHP01-10, 61.1 per cent of *n* predictions are under 10 while 87.9 per cent of the *n* estimates for site GMGS2-W08 are higher than 10.

It is noteworthy that *n* predictions at sites NGHP01-10 and GMGS2-W08 are far beyond the range suggested by previous laboratory measurements for hydrocarbon-bearing samples (e.g. Schön 1996). We assume it could result from the unusual behaviour of hydrate at sites NGHP01-10 and GMGS2-W08: hydrates primarily present in the fractures, and therefore, they grow following a certain direction, turning the sediment into an anisotropic medium which few laboratory works have investigated.

Hence, we propose a new theoretical approach to interpret the *n* values from sites NGHP01-10 and GMGS2-W08. For both fracture-filling sites the electrical property for *n* calibration was RING resistivity logged during drilling. This logging-while-drilling tool was located directly above the drill bit and used two transmitter coils and a number of electrodes to obtain several resistivity measurements. The upper and lower transmitter coils produce currents in the collar that meet at the ring electrode (Collett *et al.* 2015). In a vertical well with vertical fractures such as sites NGHP01-10 and GMGS2-W08, these currents would generally propagate perpendicularly to the borehole and fracture planes (Cook *et al.* 2010). Consequently, sediment hosting vertical-fracture-filling hydrate can be seen as a series configuration of hydrate-free layer and hydrate layer in terms of resistivity measurement, that is, a hydrate free sediment layer on top of a hydrate filled layer. Eq. (4) below can be used to demonstrate the formation resistivity R_t:

$$R_t = R_{hyd} V_{hyd} + R'_0(1 - V_{hyd}), \tag{4}$$

where R_{hyd} and V_{hyd} represent the resistivity and volume fraction of vein-like hydrate, respectively. Slightly different from the background resistivity R_0 in Section 3, R'_0 is not the resistivity of the

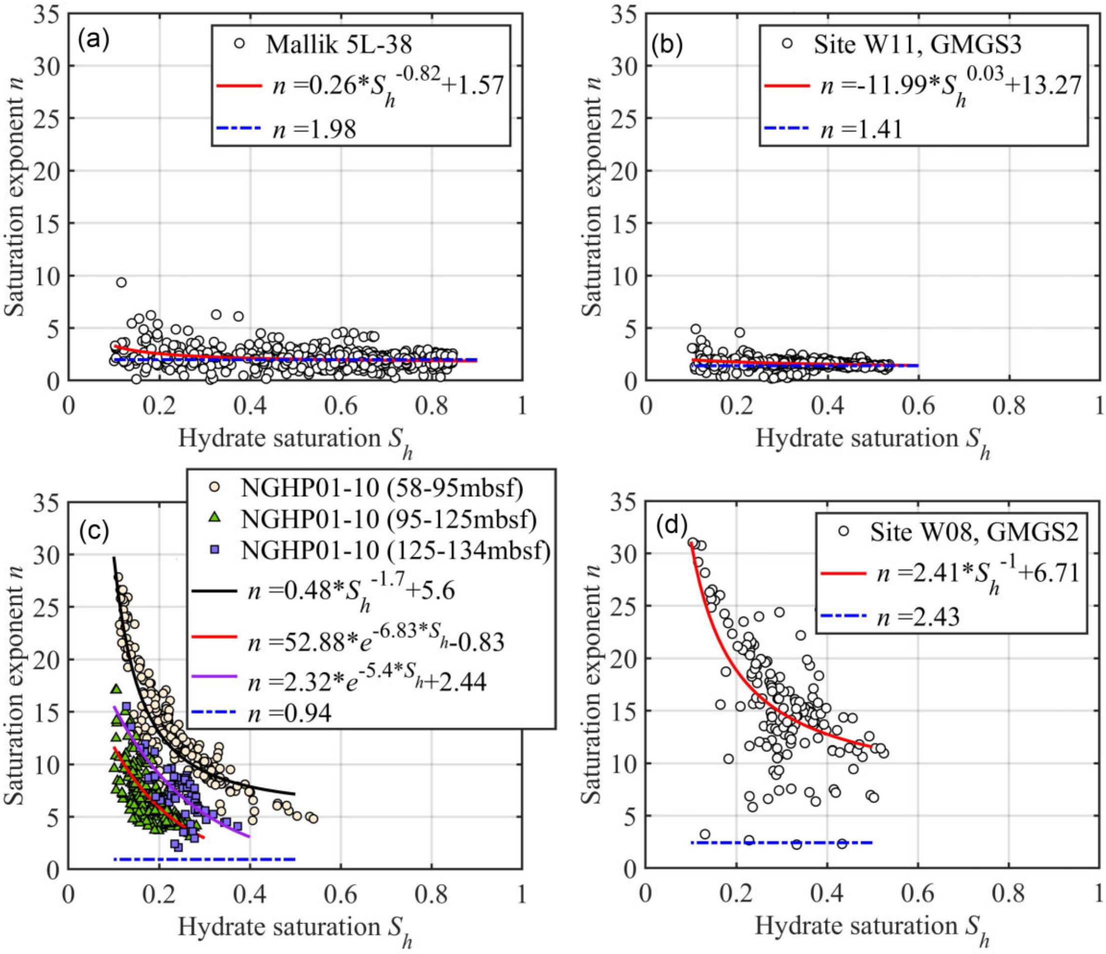

Figure 5. The saturation exponent versus hydrate saturation at sites (a) Mallik 5L-38 (fluid-displacing), (b) W11, GMGS3 (fluid-displacing), (c) NGHP01-10 (fracture-filling) and (d) W08, GMGS2 (fracture-filling). We tried three fitting strategies, linear, power function and exponential function regression for all four sites. *R*-squared values for *n* estimates are shown in Table 3. The solid lines are the fitting results with the largest *R*-squared values.

Table 3. *R*-squared values for regression results of saturation exponent at four sites.

Sites	Intervals (mbsf)	R^2 for a linear function ($n = aS_{\mathrm{h}} + b$)	R^2 for a power function ($n = aS_{\mathrm{h}}{}^{b} + c$)	R^2 for a exponential function ($n = ae^{bS_{\mathrm{h}}} + c$)
Mallik 5L-38	891–931 942–993 1069–1107	0.070	0.087	0.073
W11, GMGS3	116–201	0.053	0.067	0.056
NGHP01-10	58–95	0.597	0.762	0.698
	95–125	0.526	0.554	0.560
	125–134	0.514	0.557	0.562
W08, GMGS2	65–98	0.307	0.375	0.338

whole rock with the hydrate part replaced by brine, but only denotes the resistivity of the hydrate-free part within the *in situ* sediment. Since the hydrate veins displace and compact the surrounding sediment during hydrate growth (Spangenberg 2001), the ϕ used for deriving R_0' (see eq. 1) is no longer the initial porosity of the sediment ϕ_{initial} (void volume prior to the hydrate presence) but instead the porosity ϕ is given by the expression

$$\phi = \frac{\phi_{\mathrm{initial}}\,(1 - S_{\mathrm{h}})}{1 - \phi_{\mathrm{initial}} S_{\mathrm{h}}}. \tag{5}$$

In this work ϕ_{initial} is defined as the average of porosities derived from density logs. Moreover, the resistivity of pure hydrate R_{hyd} in eq. (4) is debatable. Laboratory results from Davidson (1983) indicated that synthetic pure methane hydrate could be a highly electrical resistive medium, while Camps *et al.* (2008) demonstrated hydrate decreases the bulk resistivity as fluid ions excluded from the hydrate structure during hydrate formation can promote an interconnected network of saline pore channels. Based on previous studies, Cook *et al.* (2010) loosely constrained the R_{hyd} for fracture-filling hydrate in the Krishna-Godavari Basin by a wide interval, from 50 to 1200 Ωm. Herein, we model the R_{t} as a function of hydrate saturation

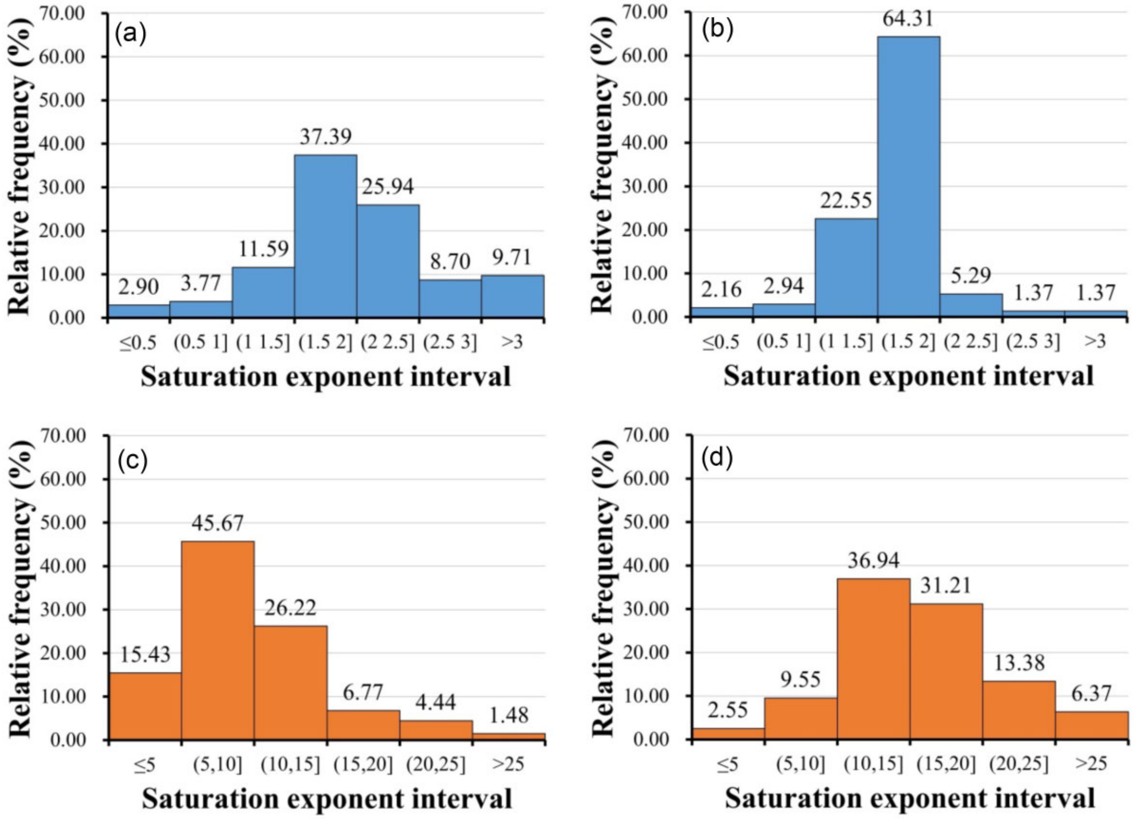

Figure 6. The distribution of saturation exponent estimates for sites (a) Mallik 5L-38 (fluid-displacing), (b) W11, GMGS3 (fluid-displacing), (c) NGHP01-10 (fracture-filling) and (d) W08, GMGS2 (fracture-filling). The label for y-axis, relative frequency, denotes the number of n values falling in a particular bin divided by the total number of n estimates.

using two exponentially growing R_{hyd} values, 1 and 1000 Ωm, and R_0' predicted by modified eq. (1). These theoretical R_{t} values then can be employed to estimate the n value from eq. (3). In this case, n can be expressed as follows:

$$n = \frac{\log\left(\frac{aR_{\mathrm{w}}}{\phi_{\mathrm{initial}}^{m}}\right) - \log\left[R_{\mathrm{hyd}}\phi_{\mathrm{initial}}S_{\mathrm{h}} + \frac{aR_{\mathrm{w}}}{\left(\frac{\phi_{\mathrm{initial}}-\phi_{\mathrm{initial}}S_{\mathrm{h}}}{1-\phi_{\mathrm{initial}}S_{\mathrm{h}}}\right)^{m}}\right]}{\log(1-S_{\mathrm{h}})}. \qquad (6)$$

We then compare these theoretical n values and n estimated from field data at sites NGHP01-10 and W08-GMGS2 (Figs 5c–d). As demonstrated in Figs 7(a) and 9, the n values predicted from field data indicate R_{hyd} values are between 1 and 1000 Ωm at both sites. Moreover, using the n expression in eq. (6) and the least-squares regression fitting strategy, we estimate the pure hydrate electrical resistivities for sites W11, GMGS3 and NGHP01-10. In Figs 7(a) and 9, the resistivity-model-derived nonlinear trends (solid lines) coincide with the n estimates from Archie's equations (circles). Furthermore, using the resistivity model for homogeneous distributed hydrates by Spangenberg (2001), we estimate four constant n (blue dashed line in Fig. 5) for all hydrate sites in this study. As shown, the resistivity-model-derived n values are quite close to the n estimates from Archie's equations at two fluid-displacing hydrate sites, but are much lower than the n estimates from Archie's equations at two fracture-filling hydrate sites. Results above further confirm that anisotropy induced by fractures is the reason why n values estimated at sites NGHP01-10 and W08-GMGS2 follow a nonlinear trend and are much higher than the n suggested by previous studies on fluid-displacing hydrate.

At site NGHP01-10, the trends between n and hydrate saturation within 58–95 mbsf (Interval I), 95–125 mbsf (Interval II) and 125–134 mbsf (Interval III) are quite distinct. To test whether differences in fracture dip angles can possibly contribute to these multiple trends, in Fig. 7(b) we show the n values for samples with different fracture dips, in which the fracture dips were estimated using Schlumberger's GeoFrame log analysis software. However, no obvious relationship between the fracture dip and n value can be observed. On the other hand, using the n expression in eq. (6) and the least-squares regression fitting strategy, we estimated the pure hydrate electrical resistivities for Intervals I–III. As shown in Fig. 7(c), the hydrate resistivity estimated from Interval I is the highest among the three, followed by Intervals III and II.

We speculate that different trends among Intervals I–III are possibly caused by the distinct gas compositions of hydrate. Organic geochemical studies show that abundant CH_4 and CO_2 gas were collected from site NGHP01-10, and the concentration of CH_4 gas from headspace for core samples is 0.37 to 5.13 times that of CO_2 gas within 58–134 mbsf (Collett *et al.* 2015). Assuming that CH_4 and CO_2 are the main gas components within hydrates, the proportion of CO_2 in the gas mixture generally varies from 25 per cent to 75 per cent according to the concentration data. In this case, the formation of CO_2 hydrate is possible, since the hydrostatic pressure and temperature at interval 58–134 mbsf are above the phase boundaries for CO_2 and CH_4 gas hydrates (as indicated in Fig. 8). Moreover, we calculate the ratio of CH_4 to CO_2 gas concentration from headspace for core samples and show the corresponding n in Fig. 7(c). As depicted, n for samples with high gas concentration ratio coincides with the trend calculated with high

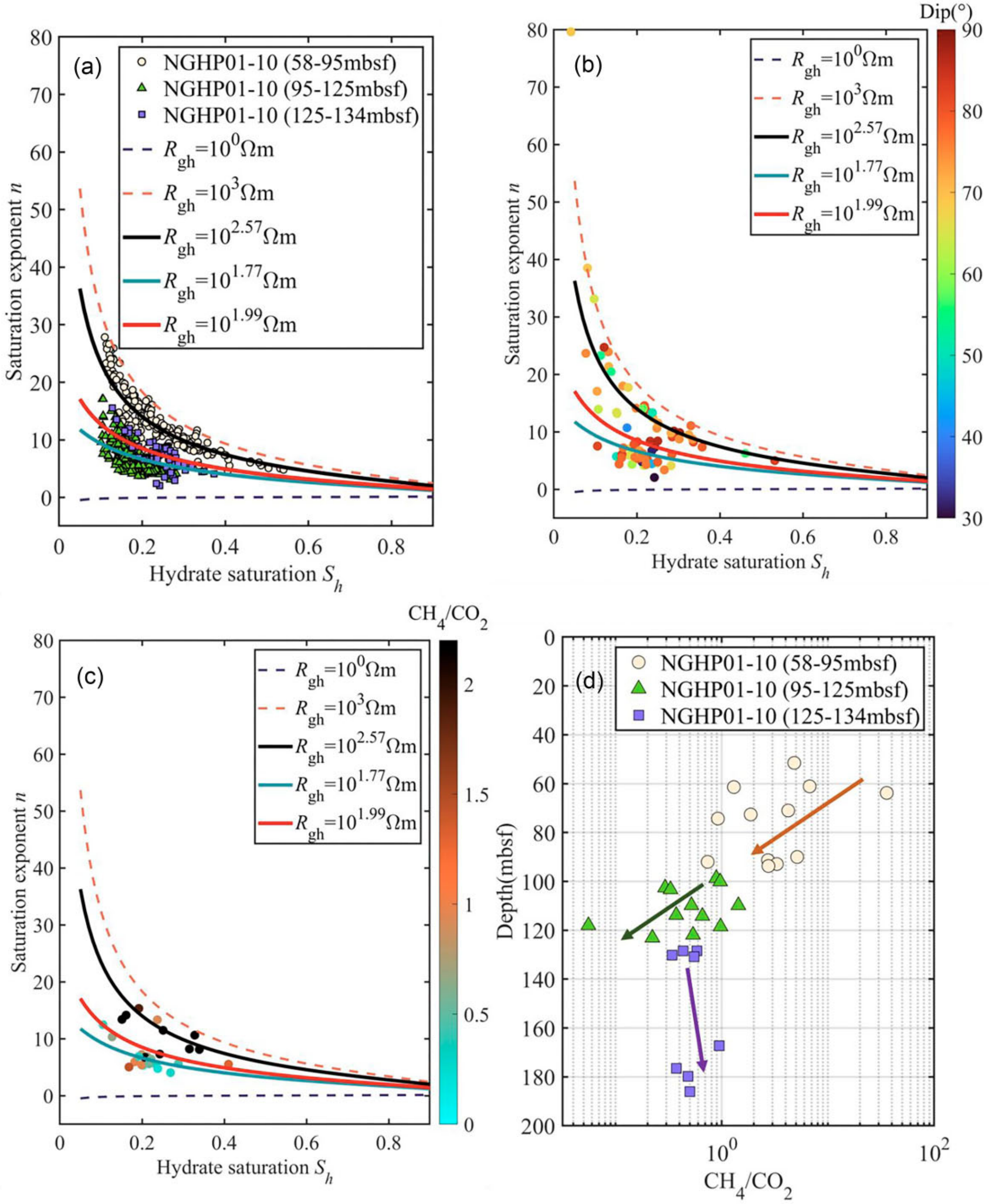

Figure 7. Saturation exponents predicted by the model and measurements at fracture-filling site NGHP01-10. (a) saturation exponents within Intervals I–III. (b) saturation exponents for samples with different fracture dips. (c) saturation exponents for samples with different ratios of CH_4 to CO_2 gas concentration. (d) the ratio of CH_4 to CO_2 gas concentration versus depth. Curves in (a–c) represent the saturation exponent calculated from eq. (6) using various pure hydrate resistivity. The best pure hydrate resistivities estimated from Intervals I–III are $10^{2.57}$, $10^{1.77}$ and $10^{1.99}$, respectively.

hydrate resistivity. We think the reason for that is the difference between CH_4 hydrate and CO_2 hydrate resistivities: CH_4 hydrate exhibits much higher electrical resistivity than CO_2 hydrate (Lim *et al.* 2017; Stern *et al.* 2021). We also analyse the variation of gas concentration ratio vesus depth. In Fig. 7(d), the mean of ratio for Interval I is the highest, followed by Intervals III and II, which are consistent with the results of estimated hydrate resistivities in Fig. 7(a).

6 DISCUSSION

Fig. 4 show anomalous porosity log which has porosities up to 100 per cent. These density-derived porosities are probably too high, may be due to free gas which is not accounted for in the log-interpretation, this is why the background velocities and resistivities are lower than one would expect from the general trend of velocity and resistivity with depth. Moreover, low background velocities

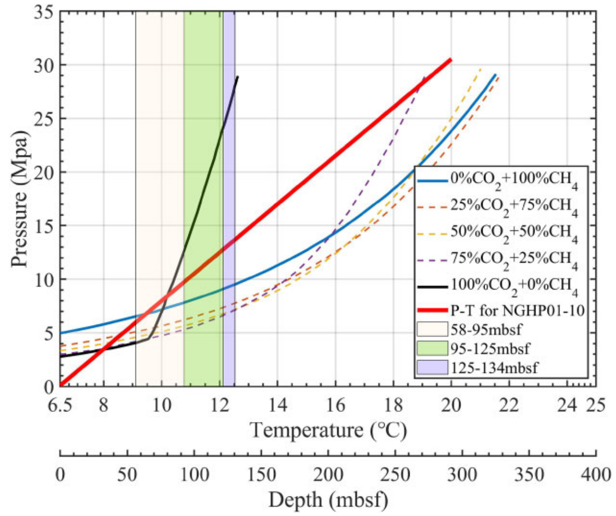

Figure 8. Hydrate phase boundary of CO_2 and CH_4 gas mixture at different compositions predicted by PVTsim (modified from Aminnaji *et al.* 2024). Red line shows the hydrostatic pressure and temperature at different depth at site NGHP01-10. Reservoir temperature is estimated using seafloor temperature and geothermal gradient shown in Table 2.

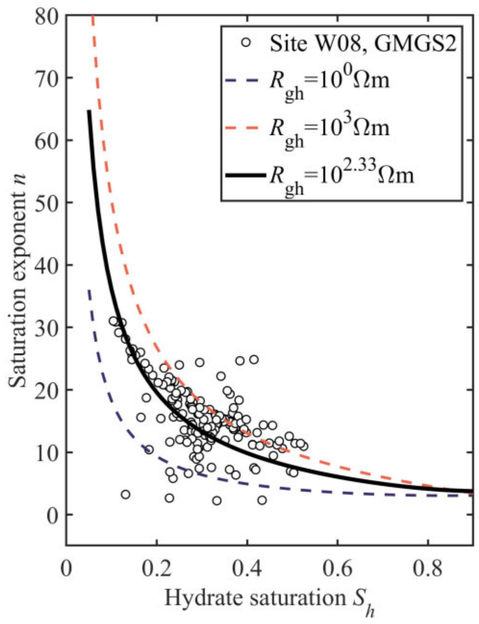

Figure 9. Saturation exponents predicted by the model and measurements at fracture-filling site W08, GMGS2. Curves represent the theoretical saturation exponent calculated with various assumptions on resistivity of the pure hydrate layer. The best pure hydrate resistivity for all samples is $10^{2.33}$.

between 56 and 63 mbsf are actually caused by a carbonate platform (Zhang *et al.* 2014).

Archie's equation was originally developed for isotropic media. In this study, we also use the Archie theory to derive the n for anisotropic sediments at sites NGHP01-10 and GMGS02-W08 where hydrates exist as sub-vertical veins. Therefore, n estimates of these two sites are the 'apparent' saturation exponents. We also note that the works of Kennedy & Herrick (2004), who demonstrated theoretically the electrical anisotropy induced by the heterogeneous laminated medium, may be less viable for interpretation of n within fracture-filling hydrate-bearing sediment, since some parameters in this theory (e.g. saturation and cementation exponents for pure hydrate layer) are difficult to determine.

Classic petrophysics holds that the Archie saturation exponent, n, is constant for a given clean sample of reservoir rock (i.e. Archie experimental conditions). However, a number of cases have indicated n can vary with pore water saturation (e.g. Swanson 1985; Longeron *et al.* 1989). In this study, we performed a comprehensive analysis of velocity and resistivity logs collected from four hydrate reservoirs, showing that n can decrease with the hydrate content, especially when hydrate forms or fills in vertical fractures. As a result, significant errors will occur if a constant n is still adopted to estimate the hydrate saturation from resistivity. For example, for four data sets used in this work, if we assume an intermediate I_R (shown as green lines parallel to the X-axis in Fig. 10), the use of a fixed n can result in over 20 per cent deviation in S_h or S_w predicted from resistivity (as shown by ΔS_w). Specifically, the ΔS_w values for sites Mallik 5L-38 and GMGS3-W11 reach 31 per cent and 20 per cent, respectively. The ΔS_w values at sites NGHP01-10 and GMGS2-W08 are 30 per cent and 25 per cent, respectively.

6.1 Factors affecting the estimated saturation exponent

It should be noted that the dependence of n on hydrate morphology and concentration can be affected by various non-hydrate factors. For example, uncertainties from the variables and parameters involved in eq. (3) may influence the n estimates. Furthermore, clay minerals within host sediment may contribute to the rock electrical conductivity (Waxman & Smits 1968; Ruffet *et al.* 1995; Schön 1996; Revil & Glover 1998), complicating the saturation exponent.

6.1.1 Surface conductivity through clay particles

Presence of clays can complicate electrical conductivity in shaly sands. Excess ions in a diffuse double layer around clay particles provide current conduction pathways along the clay surface in addition to the current flow by ions diffusing through the pore fluid (Schön 1996; Mavko, Mukerji & Dvorkin 1998). Given that conductivity of such clay surface layers relies on the brine conductivity, the relationship between the overall conductivity of saturated shaley rock and brine conductivity is no longer the linear function demonstrated by original Archie's law (eq. 3). A number of conductivity models have been proposed to account for this composite conductivity within partial-brine-saturated shaley sands, among which Worthington (1985) summarized the models used in well logging. However, most of these downhole-measurement-based models are unable to provide physical insights and a complete illustration of conductivity for all ranges of brine conductivity, except for the Waxman–Smits model (Waxman & Smits 1968) and its modifications. Here we choose this Waxman–Smits theory to account for both surface and bulk conduction:

$$n = \frac{\log(FR_w) - \log(R_t) - \log((1 + R_w B Q_v/(1 - S_h)))}{\log(1 - S_h)}, \quad (7)$$

$$B = 4.6\left(1 - 0.6e^{-1/(1.3R_w)}\right), \quad (8)$$

$$Q_v = \frac{\mathrm{CEC}\,(1 - \phi)\,\rho_g}{\phi}, \quad (9)$$

where CEC is the cation exchange capacity and ρ_g is the density of host sediment grain. The formation factor $F = \frac{a}{\phi^m}$. B denotes the average mobility of the ions.

In Fig. 11 we compare the saturation exponents estimated from

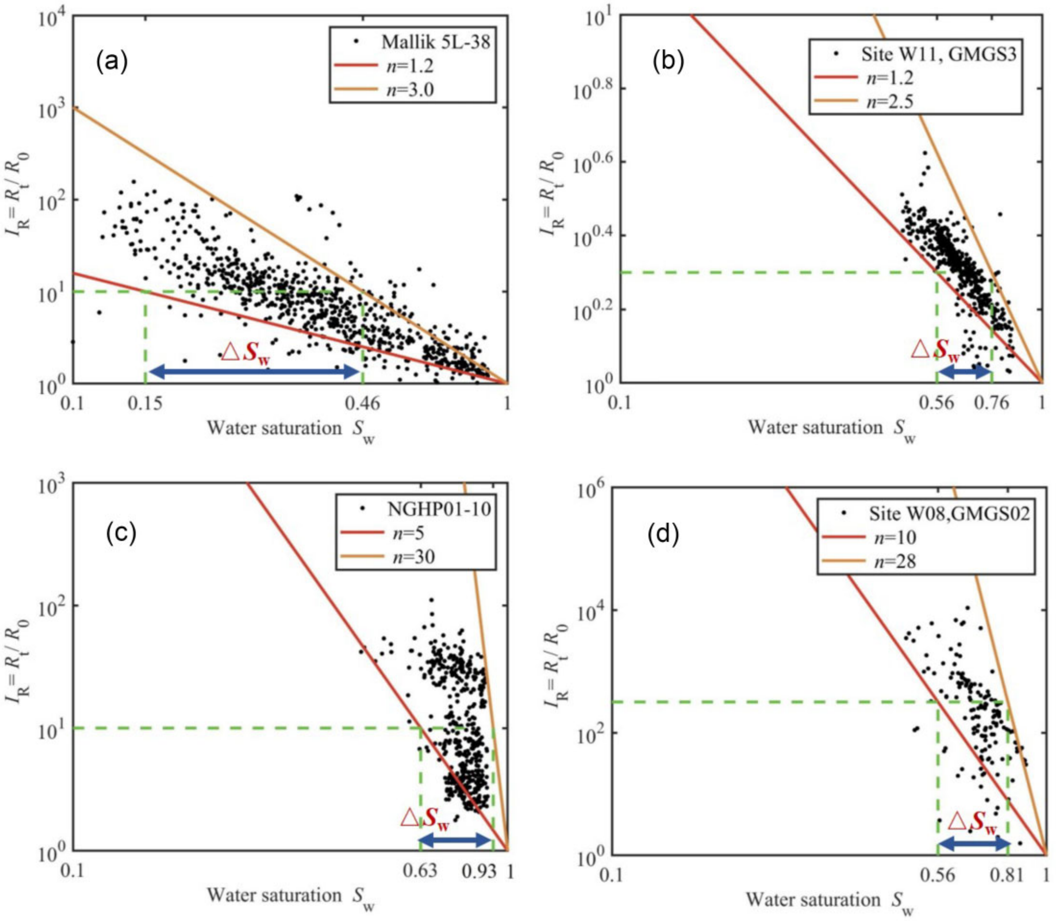

Figure 10. Potential deviation in water saturation (or hydrate saturation) resulted from an erroneous n at sites (a) Mallik 5L-38 (fluid-displacing), (b) W11, GMGS3 (fluid-displacing), (c) NGHP01-10 (fracture-filling) and (d) W08, GMGS2 (fracture-filling). The intermediate I_R values used in (a–d) (see horizontal green lines) are 10, $10^{0.3}$, 10 and $10^{2.5}$, respectively.

the original Archie's law (eq. 3) and from our modified theory (eqs 7–9). As shown, the clay-effect-considered n is slightly higher than the bulk-conduction-only n. We can explain it by eq. (3): clay layers can provide additional charge carriers, decreasing the background resistivity and elevating the associated n estimates. Eq. (3) also indicates the impact of the conductivity of clay particle on the n reduces with the increasing hydrate content, which can be one of the reasons why n is more dispersed under lower hydrate saturations at all four sites. In addition, the host sediment of fracture-filling hydrate tends to be more shaley than that of fluid-displacing hydrate due to the nature of hydrate formation (Dai *et al.* 2012). This appears to contradict the fact that gaps between n values calculated from two empirical equations (triangles in inset of Fig. 11) are more significant at two fluid-displacing hydrate sites. In fact, these gaps in n estimates only depend on the relationship between the pore water conductivity and intrinsic surface conductivity: the more significant the former is than the latter, the more negligible the clay effect is (Revil *et al.* 2014). Overall, for the four sites in this study, the surface conductivity does not significantly change the dependence of n on the hydrate morphology as illustrated in Section 5.

6.1.2 Uncertainty in hydrate saturation estimation

To estimate saturation exponent from Archie's equations, in this work we employ rock physics models to derive hydrate saturations from velocity measurements. However, these predictive elastic models which link rock petrophysical properties to elastic properties are imperfect, which potentially results in discrepancies between the velocity-derived S_h and *in situ* S_h. Given that difference between velocity-derived S_h and reference S_h (illustrated in Section 2.2) available at three sites ranges from 1 per cent to 5 per cent, we set two biased S_h by elevating and lowering the original S_h by a constant value 5 per cent to investigate the sensitivity of n to the error in S_h estimates. From Fig. 12 we observe that, for all four sites, an underestimated S_h can lead to an overestimated n, and vice versa. Similar to surface conductivity discussed in Section 6.1.1, for fluid-displacing sites the impact of the biased S_h on the derived n also decreases with the S_h. Overall, when using a slightly deviated S_h for n estimation, the dependence of the n on the hydrate morphology, as we concluded in Section 5, remain applicable.

6.1.3 Uncertainty in background resistivity determination

Background resistivity R_0 also affects n values throughout the calculations in Section 4. Various factors can account for the potential deviation between the R_0 simulated by eq. (1) and *in situ* sediment resistivity prior to the hydrate accumulation. For example, determination of R_w in Section 3 is always an ambiguous process due to the subjective Archie parameters a and m. Herein, we investigate the sensitivity of n to the potentially biased R_0 using three

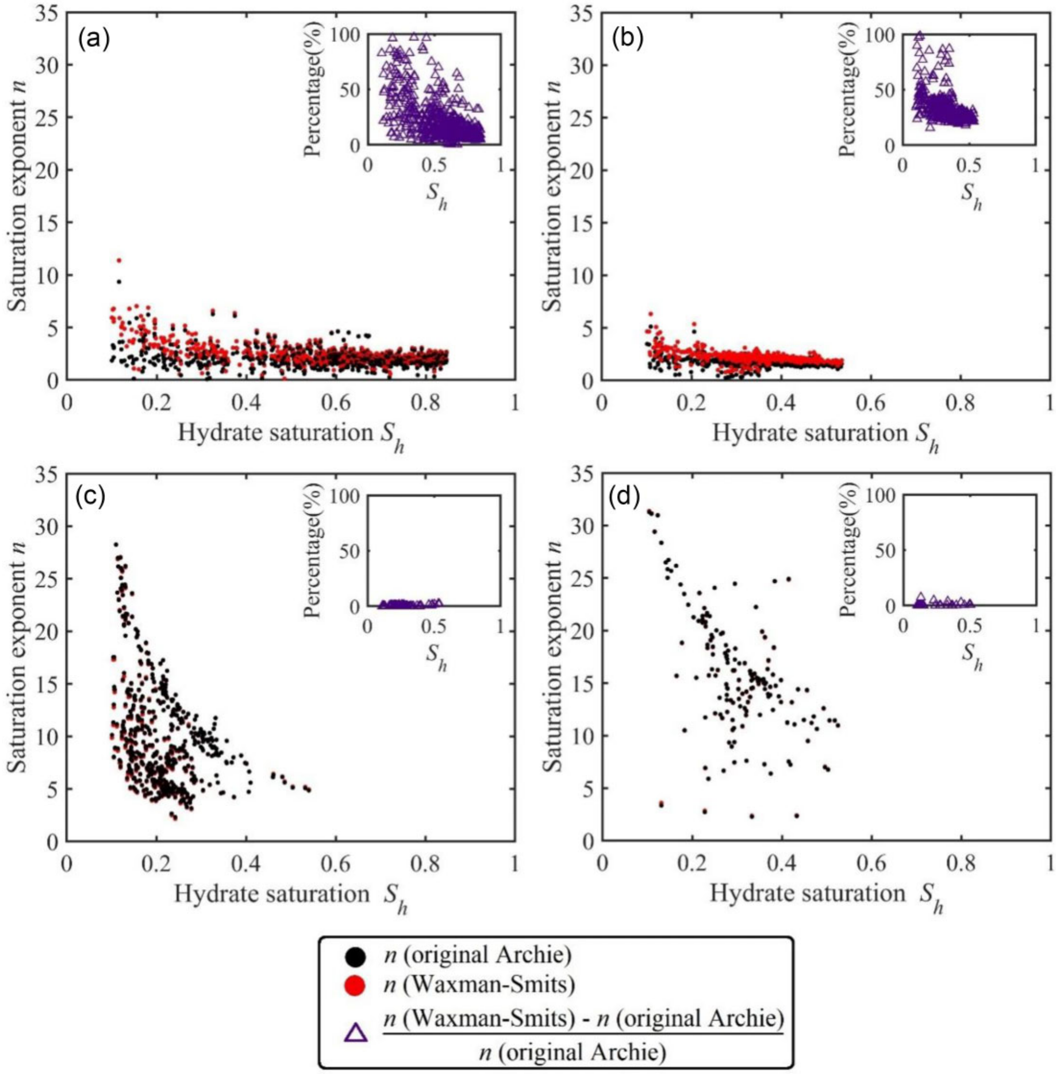

Figure 11. Effect of clay surface conductivity on saturation exponent at sites (a) Mallik 5L-38 (fluid-displacing), (b) W11, GMGS3 (fluid-displacing), (c) NGHP01-10 (fracture-filling) and (d) W08, GMGS2 (fracture-filling). Red and black dots in main figures represent saturation exponents estimated from the electrical models with Waxman-Smits theory and without (original Archie's equations) considering the clay surface conductivity, respectively. It is noted that the red dots in (c)–(d) are hardly visible because they almost superimpose on black dots. Inset figures show the percentage change of n when considering clay surface conductivity. Clay contents are obtained from gamma logs.

possible background resistivities modified from R_0. The values of n calculated using $1.1{*}R_0$, R_0 and $0.9{*}R_0$ (Fig. 13) indicates that Archie's law with underestimated background resistivity can predict a slightly higher n, and vice versa. For sites Mallik 5L-38 and W11-GMGS3 the impact of such erroneous background resistivity on the n reduces with hydrate saturation. This can be one of the reasons why n is more dispersed under lower hydrate saturation at these two fluid-displacing sites. Similar to the conductive clay particles, the effect of a biased background resistivity could be negligible compared to that from hydrate morphology (fracture-filling versus fluid-displacing).

6.2 Evidence from laboratory experiments

Controlled laboratory experiments on synthetic hydrate samples can provide insights into the physical properties of natural gas hydrate-bearing sediments and hydrate accumulation mechanisms (e.g. Sahoo *et al.* 2018b; Li *et al.* 2022). Resistivity measurements on different hydrate formation stages (i.e. multiple hydrate saturations) have been conducted in the laboratory to calibrate the saturation exponent (e.g. Schön 1996). Here, we investigate the saturation exponent using laboratory measurements on two types of host sediment: (i) synthetic fractured sandstones (Liu *et al.* 2023), and (ii) sandy sediments sample from the South China Sea (Chen *et al.* 2013). Resistivity experiments from other studies (e.g. Sahoo *et al.* 2018a; Chen *et al.* 2022) are not discussed here because (i) the sizes of these data sets are quite small, or (ii) sample resistivity was not continuously measured during the hydrate formation (i.e. data within certain hydrate saturation intervals were missing).

For the experiment conducted by Chen *et al.* (2013), the sample is the sandy sediment from the South China Sea with a particle size of 60–100 mesh. The pore fluid prior to the hydrate presence was 3.5 per cent salinity water. Methane hydrate was formed under a constant temperature of 5.6 °C and a differential pressure of

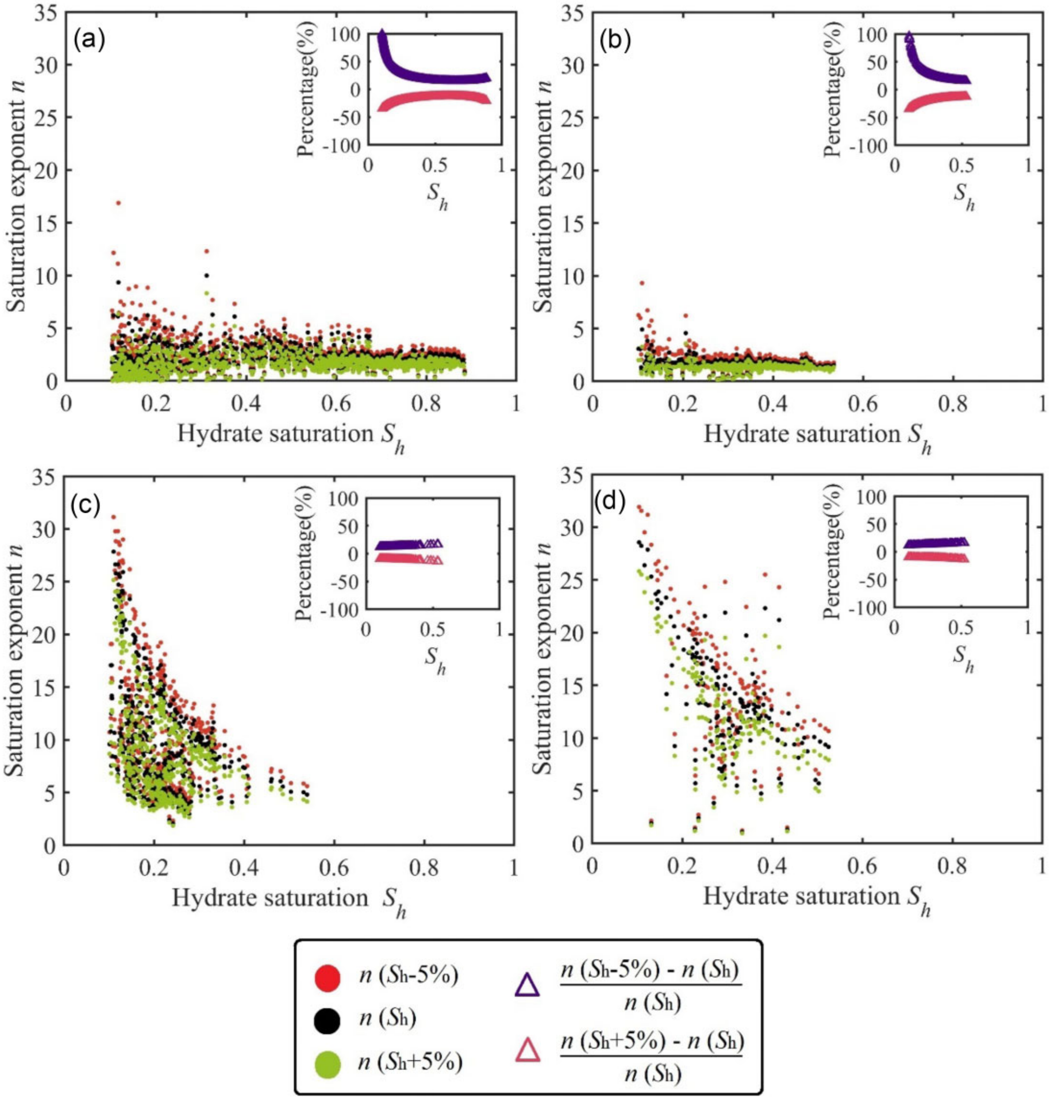

Figure 12. The effect of uncertainty of velocity-derived hydrate saturation on saturation exponent at sites (a) Mallik 5L-38 (fluid-displacing), (b) W11, GMGS3 (fluid-displacing), (c) NGHP01-10 (fracture-filling) and (d) W08, GMGS2 (fracture-filling). Saturation exponents in main figures are estimated with original or modified velocity-derived S_h. Inset figures show the percentage change of n due to S_h uncertainty.

7.27 MPa. Using the original Archie's law (eq. 3), the saturation exponent was estimated for the hydrate-bearing sediment with S_h ranging from 0 per cent–45 per cent. Fig. 14 depicts the variation of n with the hydrate saturation S_h. As shown, n experiences a slight fluctuation at low saturations. Once hydrate occupies 28 per cent of the pore space, n becomes less dependent on S_h and remains about 1.5 thereafter. The overall trend of n (linear least-squares regression line) indicates a negative dependence on the hydrate saturation, in accordance with the field evidence from sites Mallik 5L-38 and GMGS3-W11 (Figs 5a and b). However, because of the distinct host sediment properties, the empirical equation of n versus S_h is different from the results at sites Mallik 5L-38 and GMGS3-W11.

In another laboratory experiment, Liu *et al.* (2023) made silica sandstones with penny-shaped fractures (porosity, fracture density and mean grain size are about 25.7 per cent, 6.2 per cent and 0.089 mm, respectively) by placing certain paper discs on several parallel layers before compacting them into a consolidated block. Two cylindrical plugs were then cored from this block in different directions (along fracture planes and perpendicular to fractures). Here, we employ the resistivity from the sample with fracture plane perpendicular to the measurement direction, for the purpose of reproducing the natural fracture-filling hydrate which tends to fill the sub-vertical fractures (e.g. Lee & Collett 2009).

From Fig. 14 we can see that, at low S_h, n fluctuates significantly due to the possible calculation errors or temperature variations. After hydrate saturation exceeds 15 per cent, the n steadily increases from 1.03 to 2.32 (final $S_h = 30$ per cent). The overall n, completely different with the results from two fracture-filling hydrate sites (Figs 5c and d), increases with hydrate saturation. One possibility accounting for it can be the transition between various hydrate morphologies: hydrate can primarily form in the pore space at early growth stages while it gradually displaces grains in the fracture planes as saturation increases. Moreover, saturation exponent for this hydrate-bearing fractured sandstone varies within a much narrower and lower interval compared to the field results (Figs 5c and

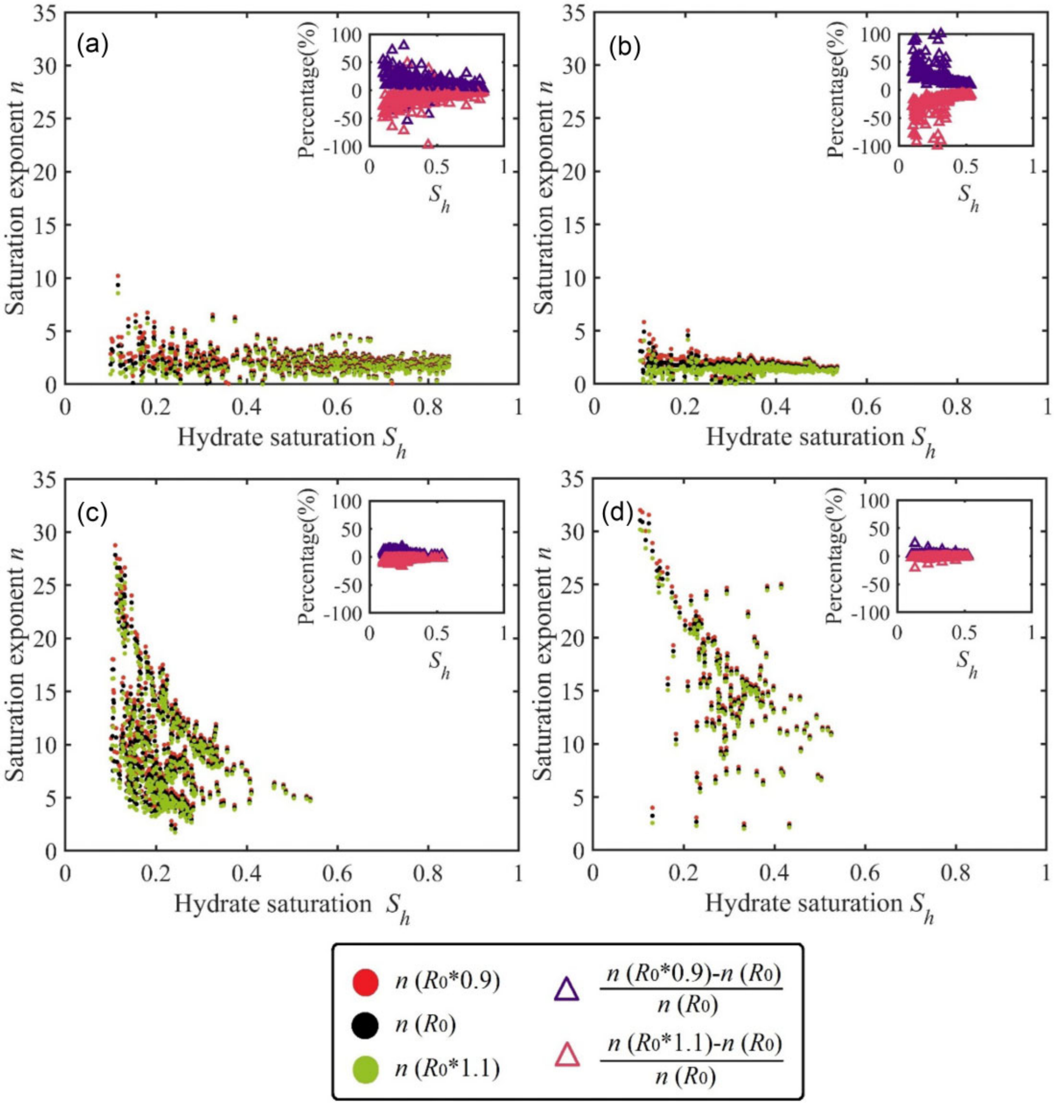

Figure 13. Effect of uncertainty of background resistivity on saturation exponent at sites (a) Mallik 5L-38 (fluid-displacing), (b) W11, GMGS3 (fluid-displacing), (c) NGHP01-10 (fracture-filling) and (d) W08, GMGS2 (fracture-filling). Saturation exponents in main figures are estimated with original or biased R_0. Inset figures show the percentage change of n due to R_0 uncertainty.

d). A possible explanation for such discrepancy is the distinct mechanisms of fractures in host sediments for natural and synthetic hydrates. Field evidence indicates fractures in natural-hydrate-bearing sediment can be formed when the capillarity force between hydrate and fluid phases exceeds effective pressure (Dai *et al.* 2012); therefore, they are usually fully saturated with natural hydrates. In contrast, fractures within the artificial sample of Liu *et al.* (2023) existed prior to the hydrate formation. In this case, the hydrate may no longer (i) be the only component within the fracture space or (ii) merely accumulate within the fractures, complicating the saturation exponent. Therefore, further laboratory experiments should be designed to reproduce the fracture-filling hydrate in natural systems to gain better understanding.

7 CONCLUSIONS

In this work, we used downhole logs from sites Mallik 5L-38, GMGS3-W11, NGHP01-10 and GMGS2-W08 to illustrate the dependence of Archie's saturation exponent n on two gas-hydrate-related factors, hydrate saturation and hydrate morphology. We obtained three power function trends, $n = 0.26 * S_{\mathrm{h}}^{-0.82} + 1.57$, $n = -11.99 * S_{\mathrm{h}}^{-0.03} + 13.27$ and $n = 2.41 * S_{\mathrm{h}}^{-1} + 6.71$ for sites Mallik 5L-38, W11-GMGS3 and W08-GMGS2, respectively. For site NGHP01-10 we obtained a power function trend $n = 0.48 * S_{\mathrm{h}}^{-1.7} + 5.6$ for intervals from 58 to 95 mbsf, and two exponential functions $n = 52.88 * e^{-6.83 * S_{\mathrm{h}}} - 0.83$ and $n = 2.32 * e^{-5.4 * S_{\mathrm{h}}} + 2.44$ for 95–125 and 125–134 mbsf, respectively. These results indicate n decreases with the hydrate saturation in both cases,

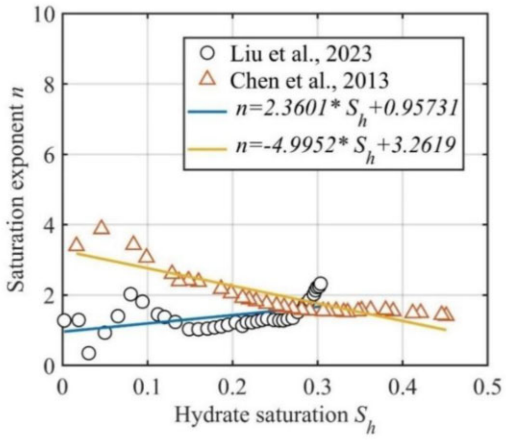

Figure 14. Laboratory evidence of the dependence of saturation exponent on hydrate saturation. Measurements in a synthetic sandstone sample with aligned fractures (Experiment I, Liu *et al.* 2023) and a sample of South China Sea sandy sediment (Experiment II, Chen *et al.* 2013) are shown as black circles and red triangles, respectively. Linear least-squares regression fitting results are shown as different coloured lines. Correlation coefficients for regression results of Experiment I and II are 0.2528 and 0.7943, respectively.

becoming more pronounced when hydrates fill vertical fractures, for example, sites NGHP01-10 and GMGS2-W08. Moreover, resistivity measurements from sites with fine grained sediments or vertical-fracture-filling hydrates yield more dispersed and larger n compared to those from sites with coarse grained sediments with fluid-displacing hydrate (Mallik 5L-38, GMGS3-W11). The reason for that is possibly the fracture-induced-anisotropy. Therefore, when using Archie's equation for hydrate saturation estimation, we recommend a variable n, depending on hydrate morphology and concentration.

We also estimate the n value from available continuous-recorded data collected during the formation of synthetic hydrates. For fluid-displacing hydrates, the n estimated from laboratory experiments negatively correlates with the hydrate concentration, consistent with the results from downhole measurements at sites Mallik 5L-38 and GMGS3-W11. However, because of the difference between the formation mechanisms of natural and synthetic vein-like hydrates, neither the n value nor its trend from a synthetic fractured sandstone sample accord with the results from sites NGHP01-10 and GMGS2-W08.

ACKNOWLEDGMENTS

The research work was supported by the National Key R&D Program of China (No. 2021YFC2800900) and the National Natural Science Funding (No. 52474076). The authors thank the cruise group and scientist parties in expeditions of GMGS2, GMGS3, NGHP01 and members associated with Mallik program for collecting and sharing the downhole measurements used in this paper. XZ acknowledges the China Scholarship Council for financial support and the National Oceanography Centre (NOC), Southampton, UK, for hosting his academic visit.

SKS acknowledges the Short-Term Scientific Mission (STSM) of COST Action ES1405 (MIGRATE) for funding his visit to GFZ, Germany, which initiated this study. He also thanks Klaus and Erik for their support during his stay at GFZ. Furthermore, SKS was funded by the NOC–RISC project P11828 'Fluid Permeability.'

DATA AVAILABILITY

The downhole measurements, velocity-derived hydrate saturation and corresponding saturation exponent presented in this study are available from https://doi.org/10.5281/zenodo.15301421.

REFERENCES

Aminnaji, M. *et al.*, 2024. CO_2 gas hydrate for carbon capture and storage applications—Part 1, *Energy,* **300,** 131579.

Archie, G.E., 1942. The electrical resistivity log as an aid in determining some reservoir characteristics, *Trans. Am. Inst. Mining Metall. Eng.,* **146,** 54–62.

Arp, J.J., 1953. The effect of temperature on the density and electrical resistivity of sodium chloride solutions, *Trans. Am. Inst. Min. Metall. Pet. Eng.,* **198,** 327–330.

Booth, J.S., Winters, W.J., Dillon, W.P., Clennell, M.B. & Rowe, M.M., 1998. Major occurrences and reservoir concepts of marine clathrate hydrates: implications of field evidence, *Geol. Soc. London, Special Publ.,* **137**(1), 113–127.

Camps, A.P., Jackson, P.D., Williams, J.F., Milodowski, A.E., Lovell, M.A. & Rochelle, C.A., 2008. Low-resistance brine pathways through Cascadia Margin sediment-hosted hydrates, in *Paper presented at the SPWLA 49th Annual Logging Symposium,* Society of Petrophysicists and Well Log Analysts, Austin, p. SPWLA–2008-FFF

Chen, Q. *et al.*, 2022. Experimental apparatus for resistivity measurement of gas hydrate-bearing sediment combined with x-ray computed tomography, *Rev. Sci. Instrum.,* **93**(9), 094708.

Chen, Y.F., Li, D.L., Liang, D.Q., Zhou, X.B. & Wu, N.Y., 2013. Relationship between gas hydrate saturation and resistivity in sediments of the South China Sea, *Acta Petrol. Sinica,* **34**(3), 507–512.

Clennell, M.B., Hovland, M., Booth, J.S., Henry, P. & Winters, W.J., 1999. Formation of natural gas hydrates in marine sediments: 1. Conceptual model of gas hydrate growth conditioned by host sediment properties, *J. geophys. Res.,* **104**(B10), 22 985–23 003.

Coates, G.R., Xiao, L. & Prammer, M.G., 1999. *NMR Logging: Principles and Applications,* Haliburton Energy Services. Available at: https://www.vista-clara.com/wp-content/uploads/2020/10/NMRLoggingPrinciples-10.1.1.206.319.pdf

Collett, T. *et al.*& the NGHP Expedition Scientists, 2015. *Indian National Gas Hydrate Program Expedition 01 Report: U.S,* Geological Survey Scientific Investigations Report 2012–5054, U.S. Geological Survey, 1442 p.

Collett, T.S. & Dallimore, S.R., 1998. Quantitative assessment of gas hydrates in the Mallik L-38 well, Mackenzia Delta, N.W.T., Canada, in *Proceedings of the 8th International Conference on Permafrost,* Yellowknife, Northwest Territories, p. 189–194.

Collett, T.S., Goldberg, D.S., Janik, A. & Guerin, G., 2003. Downhole log assessment of gas hydrate and free-gas concentrations on Hydrate Ridge, *AGU Fall Meeting Abstracts,* **2003,** OS51C–0876.

Collett, T.S., Johnson, A.H., Knapp, C.C. & Boswell, R., 2009. Natural gas hydrates: a review, in *Natural Gas Hydrates—Energy Resource Potential and Associated Geologic Hazards: AAPG Memoir, Vol. 89,* pp. 146–219, eds Collett, T., Johnson, A., Knapp, C. & Boswell, R., eds., American Association of Petroleum Geologists.

Collett, T.S. & Lee, M.W., 2005. Electrical-resistivity well-log analysis of gas hydrate saturations in the JAPEX/JNOC/GSC et al. Mallik 5L-38 gas hydrate production research well, in *Scientific Results from the Mallik 2002 Gas Hydrate Production Research Well Program, Mackenzie Delta, Northwest Territoties, Canada,* eds Dallimore, S.R. & Collett, T.S., Geological Survey of Canada, Bulletin, **585,** 8.

Collett, T.S., Lewis, R.E. & Dallimore, S.R., 2005. JAPEX /JNOC/GSC et al. Mallik 5L-38 gas hydrate production research well downhole well-log and core montages, in Dallimore, S. R. & Collett, T. S., eds., *Scientific Results from the Mallik 2002 Gas Hydrate Production Research Well Program,* Mackenzie Delta, Northwest Territories, Canada: Geological Society of Canada, Bulletin 585, 23.

Cook, A.E., Anderson, B.I., Malinverno, A., Mrozewski, S. & Goldberg, D.S., 2010. Electrical anisotropy due to gas hydrate-filled fractures, *Geophysics,* **75**(6), F173–F185.

Cook, A.E. & Goldberg, D.S., 2008. Extent of gas hydrate filled fracture planes: implications for *in situ* methanogenesis and resource potential, *Geophys. Res. Lett.,* **35,** L15302.

Cook, A.E. & Waite, W.F., 2018. Archie's saturation exponent for natural gas hydrate in coarse-grained reservoirs, *J. geophys. Res.: Solid Earth,* **123,** 2069–2089.

Dai, J.C., Snyder, F., Gillespie, D., Koesoemadinata, A. & Dutta, N., 2008. Exploration for gas hydrates in the deepwater, northern Gulf of Mexico: part I. A seismic approach based on geologic model, inversion, and rock physics principles, *Mar. Pet. Geol.,* **25,** 830–844.

Dai, S., Santamarina, J.C., Waite, W.F. & Kneafsey, T.J., 2012. Hydrate morphology: physical properties of sands with patchy hydrate saturation, *J. geophys. Res.,* **117,** B11205.

Dallimore, S.R., Uchida, T. & Collett, T.S., 1999. Scientific results from JAPEX/JNOC/GSC Mallik 2L-38 gas hydrate research well, Mackenzie Delta, Northwest Territories, Canada, *Geol. Surv. Can., Bull.,* **544**.

Davidson, D.W., 1983. Gas hydrate as clathrate ices, in *Natural Gas Hydrates: Properties, Occurrence and Recovery,* pp. 1–16, ed. Cox, J., U.S. Department of EnergyOffice of Scientific and Technical Information.

Dvorkin, J., Helgerud, B., Waite, W.F., Kirby, S.H. & Nur, A., 2000. Introduction to physical properties and elasticity models, in *Natural Gas Hydrate in Oceanic and Permafrost Environment,* pp. 245–260, ed. Max, M.D., Kluwer Academic.

Dvorkin, J. & Nut, A., 1998. Time-average equation revisited, *Geophysics,* **63**. 460–464.

Froelich, P.N., Kvenvolden, K.A., Torres, M.E., Waseda, A., Didyk, B.M. & Lorenson, T.D., 1995. Geochemical evidence for gas hydrate in sediment near the Chile triple junction, in *Proc. ODP, Sci. Results, 141, Ocean Drilling Program,* eds Lewis, S.D., Behrmann, J.H., Musgrave, R.J. & Cande, S.C., College Station, TX, pp. 279–286.

Helgerud, M.B., Dvorkin, J., Nur, A., Sakai, A. & Collett, T., 1999. Elastic-wave velocity in marine sediments with gas hydrates: effective medium modeling, *Geophys. Res. Lett.,* **26,** 2021–2024.

Helgerud, M.B., Waite, W.F., Kirby, S.H. & Nur, A., 2009. Elastic wave speeds and moduli in polycrystalline ice ih, sI methane hydrate, and sII methane-ethane hydrate, *J. geophys. Res.,* **114,** B02212.

Hesse, R., 2003. Pore anomalies of submarine gas hydrate zones as tool to assess hydrate abundance and distribution in the subsurface. What have we learned in the past decade?, *Earth Sci. Rev.,* **61,** 149–179.

Holland, M., Schultheiss, P., Roberts, J. & Druce, M., 2008. Observed gas hydrate morphologies in marine sediments, in *6th Int. Conf. Gas Hydrates,* University of British Columbia Library, Vancouver, B.C.

International Critical Tables of Numerical Data, *Physics, Chem. and Techn.*, 1928. **3,** 79.

Kennedy, W.D. & Herrick, D.C., 2004. Conductivity anisotropy in shale-free sandstone, *Petrophysics,* **45,** 38–58.

Kim, H.S., Riedel, M., Ryu, B.J., Kim, G.Y. & Bahk, J.J., 2013. Improving gas hydrate saturation estimates using *P*-wave velocity log data by incorporating XRD-Data for detailed matrix-mineralogy definition, *Mar. Pet. Geol.,* **47,** 155–167.

Kleinberg, R.L., Flaum, C. & Collett, T.S., 2005. Magnetic resonance log of JAPEX/JNOC/GSC et al. Mallik 5L-38 gas hydrate production research well: gas hydrate saturation, growth habit, and relative permeability, *Bull. Geol. Surv. Canada,* **585,** 114.

Kvenvolden, K.A., 1993. A primer in gas hydrates, in *The Future of Energy Gases: U.S. Geological Survey Professional Paper 1570,* pp. 279–292, ed. Howell, D. G., U.S. Geological Survey.

Kvenvolden, K.A. & Lorenson, T.D., 2001. The global occurrence of natural gas hydrate, in *Natural Gas Hydrates: Occurrence, Distribution and Detection, Geophysical Monograph,* Vol. 124, pp. 3–18, eds Paull, C.K. & Dillon, W.P., American Geophysical Union.

Lee, M.W., 2007. *Velocities and Attenuations of Gas Hydrate-bearing Sediments,* Scientific Investigations Report 2007–5264, U.S. Gelogical Survey, 11p.

Lee, M.W., 2008. *Models for Gas Hydrate-bearing Sediments Inferred from Hydraulic Permeability and Elastic Velocities,* Scientific Investigations Report 2008-5219, U.S. Geol. Surv., 15pp.

Lee, M.W. & Collett, T.S., 2009. Gas hydrate saturations estimated from fractured reservoir at site NGHP-01-10, Krishna-Godavari basin, India, *J. geophys. Res.,* **114,** 261–281.

Lee, M.W., Hutchinson, D.R., Collett, T.S. & Dillon, W.P., 1996. Seismic velocities for hydrate-bearing sediments using weighted equation, *J. geophys. Res.,* **101,** 20 347–20 358.

Li, C.H. & Liu, X.W., 2016. Seismic wave attenuation in hydrate-bearing sediments based on the patchy saturation model in the Shenhu area, South China Sea, *Interpretation,* **5**(3), SM25–SM32.

Li, C.H. & Liu, X.W., 2020. Research on the estimate of gas hydrate saturation based on LSTM recurrent neural network, *Energies,* **13**(24), 6536.

Li, Y., Wu, N., Liu, C. *et al.*, 2022. Hydrate formation and distribution within unconsolidated sediment: insights from laboratory electrical resistivity tomography, *Acta Oceanol. Sin.,* **41,** 127–136.

Lim, D., Ro, H., Seo, Y.-j., Lee, J.Y., Lee, J., Kim, S.-J., Park, Y. & Lee, H., 2017. Electrical resistivity measurements of methane hydrate during N2/CO2 gas exchange, *Energy Fuels,* **31**(1), 708–713.

Liu, S.B., Han, T.C. & Fu, L.Y., 2023. Laboratory insights into the effects of methane hydrate on the anisotropic joint elastic-electrical properties in fractured sandstones, *Pet. Sci.,* **20**(20), 803–814.

Longeron, D.G., Argaud, M.J. & Feraud, J.-P., 1989. Effect of overburden pressure and the nature and microscopic distribution of fluids on electrical properties of rock samples, *SPE Form Eval,* **4**(02), 194–202.

Luo, M. & Cao, Y., 2023. Gas hydrates at seeps, in *South China Sea Seeps,* eds Chen, D. & Feng, D., Springer.

Matsumoto, R., Tomaru, H., Chen, Y.F., Lu, H. & Clark, I.D., 2005. Geochemistry of the interstitial waters of the JAPEX/JNOC/GSC et al. Mallik 5L-38 gas hydrate production research well, in *Scientific Results from the Mallik 2002 Gas Hydrate Production Research Well Program,* Mackenzie Delta, Northwest Territories, Canada, eds Dallimore, S.R. & Collett, T. S., Geological Survey of Canada, Bulletin 585, 14p.

Mavko, G., Mukerji, T. & Dvorkin, J., 1998. *The Rock Physics Handbook*. Cambridge Univ. Press.

Milkov, A.V., Claypool, G.E., Lee, Y.-J., Xu, W., Dickens, G.R. & Borowski, W.S., 2003. ODP Leg 204 Scientific Party, *In situ* methane concentrations at Hydrate Ridge, offshore Oregon: new constraints on the global gas hydrate inventory from an active margin, *Geology,* **31,** 833–836.

Pabst, W. & Gregorová, E., 2013. Elastic properties of silica polymorphs–a review, *Ceramics,* **57,** 167–184.

Paull, C.K., Matsumoto, R. & Wallace, P.J., 1996. *Proceedings of the Ocean Drilling Program, Initial Reports,* vol. **164,** 142–144, Ocean Drill. Program, College Station, Texas.

Paull, C.K. *et al.*, 2008. Origin of pockmarks and chimney structures on the flanks of the Storegga Slide, offshore Norway, *Geo Mar. Lett.,* **28,** 43–51.

Pearson, C.F., Halleck, P.M., McGuire, P.L., Hermes, R. & Mathews, M., 1983. Natural gas hydrate deposits: a review of *in situ* properties, *J. Phys. Chem.,* **87**(21), 4180–4185.

Qian, J., Wang, X.J., Collett, T.S., Dong, D.D., Guo, Y.Q., Su, P.B. & Liang, J.Q., 2017. Gas hydrate accumulation and saturations estimated from effective medium theory in the eastern Pearl River Mouth Basin, South China Sea, *Interpretation,* **5**(3), SM33–SM48.

Qian, J., Wang, X.J., Collett, T.S., Guo, Y.Q., Kang, D.J. & Jin, J.P., 2018. Downhole log evidence for the coexistence of structure II gas hydrate and free gas below the bottom simulating reflector in the South China Sea, *Mar. Pet. Geol.,* **98,** 662–674.

Revil, A. & Glover, P.W.J., 1998. Nature of surface electrical conductivity in natural sands, sandstones, and clays, *Geophys. Res. Lett.,* **25**(5), 691–694.

Revil, A., Kessouri, P. & Torres-Verdín, C., 2014. Electrical conductivity, induced polarization, and permeability of the Fontainebleau sandstone, *Geophysics,* **79**(5), D301–D318.

Riedel, M., Long, P.E. & Collett, T.S., 2006. Estimates of *in situ* gas hydrate concentration from resistivity monitoring of gas hydrate bearing sediments during temperature equilibration, *Mar. Geol.,* **227,** 215–225.

Ruffet, C., Darot, M. & Guéguen, Y., 1995. Surface conductivity in rocks: a review, *Surv. Geophys.,* **16,** 83–105.

Sahoo, S.K. & Best, A.I., 2021. The influence of gas hydrate morphology on reservoir permeability and geophysical shear wave remote sensing, *J. geophys. Res.: Solid Earth,* **126,** e2021JB022206.

Sahoo, S.K. *et al.*, 2018a. Laboratory insights into the effect of sediment-hosted methane hydrate morphology on elastic wave velocity from time-lapse 4-D synchrotron X-ray computed tomography, *Geochem. Geophys. Geosyst.,* **19,** 4502–4521.

Sahoo, S.K., Marín-Moreno, H., North, L.J., Falcon-Suarez, I., Madhusudhan, B.N., Best, A.I. & Minshull, T.A., 2018b. Presence and consequences of coexisting methane gas with hydrate under two phase water-hydrate stability conditions, *J. geophys. Res.: Solid Earth,* **123,** 3377–3390.

Santamarina, J.C. *et al.*, 2015. Hydro-bio-geomechanical properties of hydrate-bearing sediments from Nankai Trough, *Mar. Pet. Geol.,* **66**(2), 434–450.

Santamarina, J.C. & Ruppel, C., 2008. The impact of hydrate saturation on the mechanical, electrical, and thermal properties of hydrate-bearing sand, silts, and clay, in *Proceedings of the 6th International Conference on Gas Hydrates,* eds Englezos, P. & Ripmeester, J., Vancouver, Canada.

Schön, J., 1996. Physical properties of rocks fundamentals and principles of petrophysics, in *Handbook of Geophysical Exploration: Ser., Sect. I, Seismic Exploration,* Vol. **18,** 1st edn, Pergamon.

Sen, P.N., 1997. Resistivity of partially saturated carbonate rocks with microporosity, *Geophysics,* **62**(2), 415–425.

Sha, Z.B., Liang, J.Q., Zhang, G.X. *et al.*, 2015. A seepage gas hydrate system in northern South China Sea: seismic and well log interpretations, *Mar. Geol.,* **366**(8), 69–78.

Spangenberg, E., 2001. Modeling of the influence of gas hydrate content on the electrical properties of porous sediments, *J. geophys. Res.,* **106**(B4), 6535–6548.

Stern, L.A., Constable, S., Lu, R., Du Frane, W.L. & Roberts, J.J., 2021. Electrical properties of carbon dioxide hydrate: implications for monitoring CO_2 in the gas hydrate stability zone, *Geophys. Res. Lett.,* **48,** e2021GL093475.

Swanson, B.F., 1985. Microporosity in reservoir rocks-its measurement and influence on electrical-resistivity, *The Log Analyst,* **26**(6), 42–52.

Tian, D.M. & Liu, X.W., 2021. Identification of gas hydrate based on velocity cross plot analysis, *Mar. Geophys. Res.,* **42,** 11.

Wang, X.J., Wu, S.G., Lee, M., Guo, Y.Q., Yang, S.X. & Liang, J.Q., 2011. Gas hydrate saturation from acoustic impedance and resistivity logs in the Shenhu area, South China Sea, *Mar. Pet. Geol.,* **28**(9), 1625–1633.

Wang, Y., Feng, J.C., Li, X.S., Zhang, Y. & Li, G., 2016. Evaluation of gas production from marine hydrate deposits at the GMGS2-Site 8, Pearl River Mouth Basin, South China Sea, *Energies,* **9,** 222.

Waxman, M.H. & Smits, L.J.M., 1968. Electrical conductivities in oil-bearing Shaly Sands, *Soc. Pet. Eng. J.,* **8**(02), 107–122.

White, J.E., 1965. *Seismic Waves—Radiation, Transmission, and Attenuation,* McGraw-Hill, 320.

Wildenschild, D., Roberts, J.J. & Carlberg, E.D., 2000. On the relationship between microstructure and electrical and hydraulic properties of sand-clay mixtures, *Geophys. Res. Lett.,* **27**(19), 3085–3088.

Worthington, P.F., 1985. Evolution of shaley sand concepts in reservoir evaluation, *Log Analyst,* **26,** 23–40.

Worthington, P.F. & Pallatt, N., 1992. Effect of variable saturation exponent on the evaluation of hydrocarbon saturation, *SPE Form. Eval.,* **7**(4), 331–336.

Wyllie, M.R.J., Gregory, A.R. & Gardner, L.W., 1956. Elastic wave velocities in heterogeneous and porous media, *Geophysics,* **21,** 41–70.

Yu, Y.S., Zhang, X.W., Liu, J.W., Lee, Y. & Li, X.S., 2021. Natural gas hydrate resources and hydrate technologies: a review and analysis of the associated energy and global warming challenges, *Energy Environ. Sci.,* **14**(11), 5611–5668.

Zhang, G.X., Yang, S.X., Zhang, M., Liang, J.Q., Lu, J.A., Holland, M. & Schultheiss, S., and the GMGS2 Science Team, 2014. GMGS2 Investigates a rich and complex gas hydrate environment in the South China Sea: fire in the ice, *Methane Hydrate Newsl,* **14**(1), 1–5.